Universitá Cattolica del Sacro Cuore

Sede di Brescia

Facoltá di Scienze Matematiche, Fisiche e Naturali

Corso di Laurea Specialistica in Fisica

Non-equilibrium infrared optical spectroscopy of High T_C superconductors

Relatore:

Dott. Claudio Giannetti

Correlatore:

Ch.mo Prof. Fulvio Parmigiani

Laureando: **Davide Bossini**

mat. 3611044

Anno Accademico 2008/2009

First we guess it. Then we compute the consequences of the guess to see what would be implied if the law we guess is right. Then we compare the result of the computation to nature, with experiment or experience, compare it directly with observation to see if it works. If it disagrees with experiment it is wrong. In that simple statement is the key to science. It does not make any difference how beautiful your guess is. It does not make any difference how smart you are, who made the guess, or what your name is-if it disagrees with experiment it is wrong. That is all there is to it.

Richard Feynman

CONTENTS

1. INTRODUCTION

The discovery of superconductivity at high critical temperature (Bednorz and Müller, 1986) in ceramic copper oxides (*cuprates*) changed the history of a phenomenon previously confined to very low temperatures.

In spite of the intense activity in the field of the cuprates the question of the mechanism that causes the onset of superconductivity is still open. Among the various theoretical models suggested so far, some authors [34] proposed that a BCS-like pairing mechanism, with a very strong electron-boson coupling, could make the cuprates superconductors.

Many experimental works have been accomplished, in order to study the electron-phonon coupling in the high T_c superconductors [27] [28]. A time-resolved optical experiment is able to detect directly the femtosecond dynamics, which is the fingerprint of the electron-phonon interaction. However in the superconducting state this kind of measurement has never been performed, because the electron dynamics is covered by the superconducting recovery process.

In this work we report the results of an experimental observation in a superconducting cuprate, performed with optical technique. We noticed a femtosecond dynamics in our data, which we interpreted as due to the electron-phonon coupling.

The measurement was possible thanks to the tunability of the laser source, in the infrared region of the spectrum.

2. HIGH-TEMPERATURE SUPERCONDUCTIVITY

In this chapter we introduce the subject of *high temperature superconductivity*. First we report the original discovery and some experimental evidences common to all the cuprates that make them different to the standard BCS superconductors. Second we describe the approach of this work, by stating the goal of the experimental activity. We finally describe the physics of these materials: we analyze the lattice structure, the phase diagram and the electronic properties.

2.1 **The coming of a new era**

The phenomenon of superconductivity was observed for the first time in 1911 at the Leiden laboratories. While studying the temperature dependance of electrical resistivity of mercury, H. Kamerlingh-Onnes discovered that at a temperature T_c (critical temperature) in the proximity of 4 K the resistance of the sample suddenly dropped to zero.
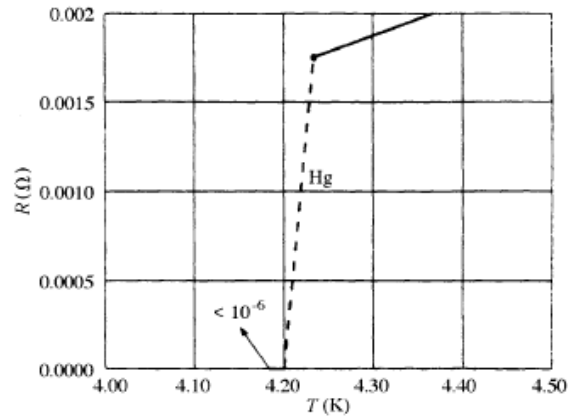
Figure 2.1: First experimental evidence of the superconducting transition. Figure from [1].

The outcome of this experiment is reported in figure (2.1). The theoretical description of this phenomenon was provided only in 1957 [3] by Bardeen, Cooper and Schrieffer (BCS). According to BCS theory, the key process occurring in superconductors is the pairing of electrons: the conducting electrons in a superconducting metal form pairs (they are bound states), known as *Cooper pairs*.

The origin of the pairing is an attraction between electrons, strong enough to overcome the Coulomb repulsion; this attraction is provided by the electron-lattice interaction or, in a quantum mechanical picture, by the electron-phonon coupling.

In 1986 the 75th anniversary of superconductivity was marked by the discovery of a new class of superconducting materials, namely, high-T_c copper oxides (usually called *cuprates*). Bednorz and Müller discovered that the LaBaCuO compound became superconducting with a critical temperature $T_c \sim 30$ K.

This experimental work opened the era of *high T_c superconductivity*, changing the history of a phenomenon that had before been confined to very low temperature (until 1986 the maximum value of T_c was limited to the 23.2 K observed in Nb_3Ge).

This unexpected result prompted intense activity in the field of copper oxides and led to the synthesis of compounds with increasingly higher T_c. The most studied cuprates are $YBa_2Cu_3O_{6+x}$ (YBCO), which has maximum $T_c \sim 93$ K, and $Bi_2Sr_2Ca_1Cu_2O_{8+x}$ with maximum $T_c \sim 95$ K. At present, the highest observed value of T_c is about 150 K and is for the $HgBa_2Ca_2Cu_3O_{8+x}$ compound under pressure.

The structure and the features of the cuprates are described in the following section; for the moment we just mention that they are strong correlated systems, hence the single-particle approach of the quantum theory of solids (in the form of one-electron band theory) cannot be the right theoretical framework of the high T_c superconductivity.

The experimental evidences common for all the cuprates, and different from the BCS materials, are:

- d-wave symmetry of the superconducting gap, revealed by Angle Resolved Photoemission Spectrocopy (ARPES) [19].

- occuring of a phase called *pseudogap* [19], in which there is a gap but the system does not exhibit superconductivity.

The BCS model doesn't account for high-T_c superconductivity, since it relies on the Fermi-liquid [37] theory which cannot be applied to the cuprates in their normal state.

Nonetheless electron-phonon coupling has a significant role in the physics of the cuprates. The BCS theory was developed in the weak-coupling limit (i.e. $\lambda \ll 1$, where λ is the electron-phonon coupling constant), and it was later extended to the strong coupling case [31] [32]. In the high T_c superconductors strong electronic correlation occur and, according to some authors [34], the electron-phonon interaction is in the strong coupling regime.

Since (section 3.2) the glue function is far from vanishing above 100 meV, which is the upper energy limit for the phonons in the cuprates, in this work we will consider the electron-boson coupling, instead of the electron-phonon coupling.

Some theoretical model and some experimental evidences [34] suggest that the high temperature superconductivity involves electron pairs formation. So far. the mechanism that provides the pairing (so the *glue* mechanism) is unknown.

Among all the suggested possibilities that can be found in the literature, we pinpoint two main streams: a group of theoretical works rely on the idea that the electronic correlations are fundamental in the onset of the superconductivity; whereas the others are based on a BCS like bosonic glue mechanism.

We mention the model of Anderson [33], namely the Resonating Valence Bond (RVB) [20] as representative of the first group. From the second group we quote the *Colloquium* of Kresin and Wolf [34], where they discuss the possibility that a strong electron-phonon coupling is the main process (but maybe not the only one) that leads to the pairs formation. In this scenario the phase transition is driven by a gain in potential energy as in BCS.

2.2 **Our approach**

The goal of this work is to study the electron-boson coupling in the superconducting cuprates, in particular we analyzed $Bi_2Sr_2Ca_{0.92}Y_{0.08}Cu_2O_{8+x}$ optimally doped (Y-Bi2212 OP). We performed a pump and probe (section 5.1) measurement with ultrashort (on the order of 100 fs) laser pulses. This technique allows to study the non-equilibrium dynamics in the sub-picosecond regime, by the detection of the reflectivity variation. The measure quantity is

$$\frac{\Delta R}{R} = \frac{R_{exc} - R_{eq}}{R_{eq}} \tag{2.1}$$

as discussed in section (5.1). This non-equilibrium dynamics is properly described by the *three-temperature model* (section 7.2), which provides a direct connection between the duration of the electronic relaxation process and the electron-phonon coupling constant. This means that it is possible to measure directly this coupling constant by performing an optical experiment. This model can be applied to high T_c superconductors in normal state.

The response of the system is different in the superconducting state: in this case a slow dynamics, on the order of 1 ps, is observed (which is called *bottleneck*). This behavior dominates over the dynamics related to the electronic thermalization with the phonon heat bath. This means that a direct optical measurement of the electron-phonon coupling constant, in the superconducting state, cannot be performed. Different experimental techniques can achieve this task [28] [27]. The phenomenological model proposed by

Rothwarf and Taylor (section 7.3) accounts for the bottleneck dynamics.

In the present work we will report a pump and probe experiment performed with spectral resolution (1200-2400 nm) on the superconducting Y-Bi2212 OP (T_c= 95 K): this system is slightly different from common Bi2212. The Yttrium doping makes the critical temperature higher, by minimizing Sr site disorder at the expense of Ca site disorder [38]. We decided to probe the optical response of the sample in this frequency range because, from a theoretical prediction reported in chapter 4, the fast electronic dynamics should be observable in the infrared region.

In our experimental activity we actually observed this behavior. From our data it is possible to give an estimation of the electron-phonon coupling constant: this information can provide a hint to understand the origin of the glue mechanism.

2.3 **Physics of the cuprates**

In this section we are going to describe some features common to all the cuprates. First we analyze the lattice structure of these compounds; second we discuss the phase diagram and the doping properties. Finally we introduce the theoretical description of the electronic properties.

2.3.1 **Lattice structure**

In figure (2.2) we report a schematic representation of the unit cell of the insulating $Bi_2Sr_2Ca_1Cu_2O_8$ (Bi2212).

As we can see from the figure the lattice structure is tetragonal. Each copper atom is surrounded by six oxygens atoms, four in the $Cu-O_2$ plane and two out of plane (which are called apical oxygens) forming octahedra (fig. 2.2).

The lattice feature common to all the cuprates is the presence of copper-oxygens $(Cu-O_2)$ layers, forming single-layer or multi-layer blocks separated from each other by the so-called *charge reservoir layers* (Bi/Sr in fig. 2.2). The cuprates can be classified according to the number N of CuO_2 planes contained within the characteristics block (N is also the number of Cu ions per formula unit). Hence there are single layer compound (e.g. LSCO), bilayer compounds (e.g. $YBa_2Cu_3O_{7+x}$ and $Bi_2Sr_2Ca_1Cu_2O_{8+x}$) and trilayer compounds ($Bi_2Sr_2Ca_2Cu_3O_{10+x}$). There is general agreement that the copper-oxygens layers plays a fundamental role in the physics of the cuprates.
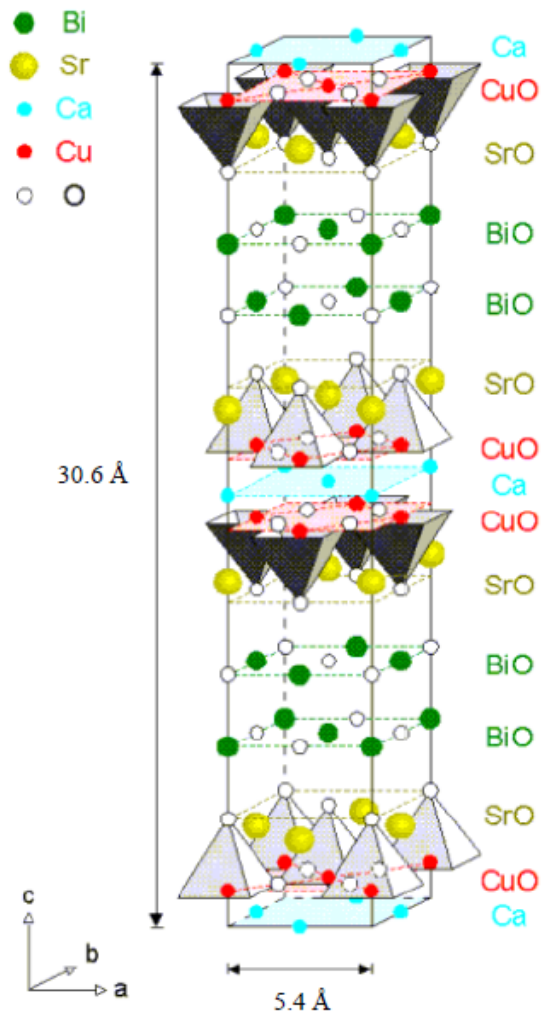
Figure 2.2: Unit cell of $Bi_2Sr_2Ca_1Cu_2O_{8+\delta}$.

2.3.2 Phase diagram

The lattice structure previously described corresponds to an insulator anti-ferromagnetic ground state. The physical properties of the cuprates can be strongly changed by injecting additional charges (electrons or holes) in these systems. This process is called *doping*. There are mainly two ways of doping charge carriers into the CuO_2 planes: by substituting different elements in

the reservoir layers or by varying the oxygen contents.

The variation of the physical properties depending on the doping concentration and temperature is expressed in the phase diagram, reported in figure (2.3) where x is the added charges concentration. By doping a cuprate electrons or holes can be added to the copper-oxygen planes, so the two sides of the phase-diagram can be explored.
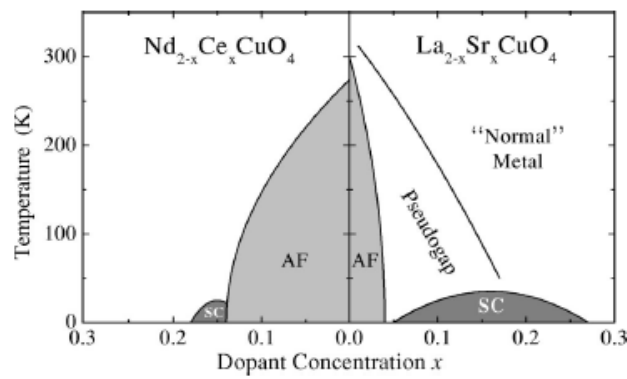
Figure 2.3: Phase diagram of n- and p-type superconductors, showing superconductivity (SC), antiferromagnetic (AF), pseudogap and normal-metal regions. Figure from [19]. The electron doped side is the left panel, while the hole doped is the right one.

Let us look at the hole doped side of figure (2.3): the antiferromagnetic order is rapidly suppressed and is completely quenched by a $3 - 5$ % hole concentration. Almost immediately after the suppression of the antiferromagnetic phase, superconductivity appears, ranging from $x = 6 - 25$ %. The dome-shaped T_c is characteristic of all hole-doped cuprates, even though the maximum T_c can significantly vary for different compounds (e.g. T_c=40 K for LSCO, T_c=95 K for BiSCO).

In the electron-doped side the antiferromagnetic phase survives up to $x = 0.14$, beyond which a region of superconductivity arises. Most of the

studies on the cuprates are performed on hole-doped samples. In fact the larger extent of the AF zone covers some peculiar features of the high-T_c superconductivity, that appear clearly in the hole-doped side of figure (2.3).

The region in the phase diagram with doping x smaller than that corresponding to the maximum T_c is the *underdoped region*. The metallic state above T_c exhibits many unusual properties not encountered before in any other metal: this region is the *pseudogap phase*. Actually it is not a well defined phase, because a definite temperature phase-boundary has not been found yet. The value of doping concentration corresponding to the maximum T_c represents the *optimally doped* condition.

Beyond optimal doping there is the *overdoped region*: the normal state in this zone show a behavior closer to a Fermi-liquid [37].

2.3.3 Electronic properties

It is generally agreed that the physics of the high-T_c superconductivity is that of the copper-oxygen layer, which is shown in figure (2.4).

Undoped compound Let us considered an undoped cuprate (which is called the parent compound, for example La_2CuO_4 is the parent compound of LSCO): in this system the formal valence of Cu is 2+, which means that the electronic state is in the d^9 configuration. The copper is surrounded by six oxygens in an octahedral environment (the apical oxygens lying above and below Cu are not shown in fig. 2.4). The apical oxygens are shifted from a perfect octahedral symmetry since the Jahn-Teller effect occurs. This phenomenon, combined with the crystal field, causes the splitting of the e_g level so that the highest partially occupied d orbital is x^2-y^2 (as it is reported
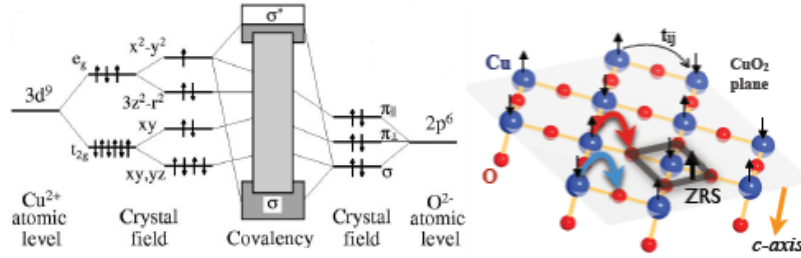
Figure 2.4: Left panel: Crystal field and Jahn-Teller splitting giving rise to the Cu-O bands. Right panel: a copper-oxygen layer, nearest neighbor copper atoms hopping (t_{ij}), charge transfer and Zhang-Rice singlet are put in evidence.

in fig. 2.4). The lobes of this orbital point directly to the p orbitals of the neighboring oxygen, forming a strong covalent bond with a large hopping integral t_{pd}.

The properties of the parent compound cannot be described by band theory: in fact in the copper-oxygen layer there is an odd number of electrons per Cu atom. According to band theory, the band is half-filled and the system must be metallic. On the contrary in the normal state the parent compound is an antiferromagnetic insulator. The reason of the band theory's failure lies in the electronic correlations (Coulombian repulsion), which make the single-particle approach unsuitable.

Electron correlations are considered within the *Mott-Hubbard model*. This theoretical framework can account for the strong repulsive energy cost of putting two electrons (or holes) on the same ion. When this energy (usually called U) dominates over the hopping energy t, the ground state is an insulator due to strong correlation effects.

In the Mott-Hubbard insulators the conduction band (so the antibonding band for the cuprates, see fig. 2.5 (c)) splits into lower and upper Hubbard
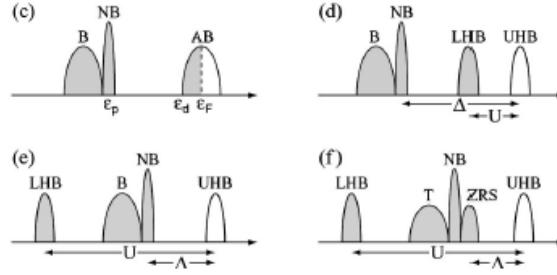
Figure 2.5: Band structure of a strongly correlated material: (c) The system is metallic in the absence of electronic correlations (3 bands: bonding, non bonding, anti-bonding); becomes (d) a Mott insulator or (e) a charge transfer insulator respectively for $\Delta >$U and U$> \Delta$; in the latter case (f) the bonding band splits into triplet and Zhang-Rice singlet.

bands (fig. 2.5 (d)) and these compounds are rather good insulators with an optical gap U of a few eV between the two Hubbard bands.

In the cuprates the description is even more difficult, because of the presence of the oxygen atoms (not accounted for in the Mott-Hubbard framework). The $d^{\,9}$ configuration is represented by energy level E_d of the Cu atom (fig.2.6) occupied by a single hole, whereas the oxygen p orbital is empty of holes and lies at energy E_p. The energy to doubly occupy E_d is U, as aforementioned, which is very large. The lowest-energy excitation is the *charge-transfer* excitation in which the hole hops from Cu d to O p. The charge-transfer energy Δ ($\Delta = E_p - E_d$) is smaller than on-site Coulomb repulsion U (fig. 2.5 (e)).

If Δ is larger than the charge-transfer integral t_{pd}, the hole will localize on the copper atom. These compounds are called *charge-transfer insulator* [36]. Experimentally an energy gap of 2 eV is observed and interpreted as the charge-transfer transition [20].
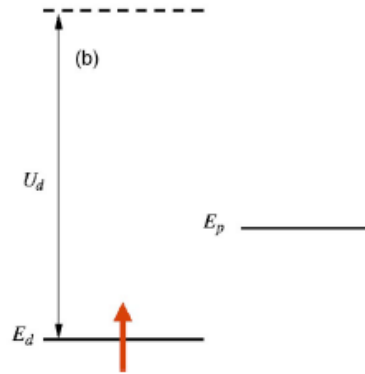
Figure 2.6: Copper d and oxygen p orbital in the hole picture. A single hole occupies the copper d orbital. The upper dashed line represents the energy level of another copper atom, the hopping requires enegy U_d.

The antiferromagnetic character of the charge-transfer insulator comes from the fact that local moments on nearest neighbor Cu prefer antiferromagnetic alignment. Thus both spins can virtually hop to the oxygen p orbital; for the Pauli principle hopping is forbidden for parallel spins. The virtual hopping process leads to an exchange interaction $J\mathbf{S}_1 \cdot \mathbf{S}_2$, where the exchange integral has value [20]

$$J = \frac{t_{pd}^4}{\Delta^3} \tag{2.2}$$

which is different from the Mott-Hubbard insulator result, namely $J = 4t^2/U$.

Single-hole doped compound   We have considered up to now undoped systems; upon doping additional holes are introduced in the CuO_2 layers. Let us consider one additional hole; it is primarily on the oxygen sites (Cu $3d$ [9]

O $2p$ [5]) and not on the copper atom, cause of the strong Coulomb repulsion. The doped hole resonates on the four oxygens sites surrounding a Cu; the spin of the hole combines with the spin of the Cu to form a spin singlet. This is known as the *Zhang-Rice singlet* [18].

The formation of such a singlet is somewhat unusual, since normally one would expect the triplet states (the spins of the two holes are parallel) to be the lowest in energy based on Hund's first rule for a Cu $3d$ [8] configuration. The singlet nature is therefore the result of the unusual properties of these materials. Zhang and Rice have proofed that the singlet configuration is the lowest energy one, by second order calculation in perturbation theory [18]. The singlet then moves through the lattice of Cu 2+ ions, without perturbing the antiferromagnetic spin ordering of Cu-O_2 planes. This is the reason why some authors [18] suggested to describe the cuprates with an effective single band hamiltonian. In principle the theoretical approach should be based on a three bands hamiltonian, in order to describe to contribution of the oxygen p and copper $d_{x^2-y^2}$ orbitals.

The single-band theory is based on the idea that the physics of the cuprates can be described by the one band Hubbard model. In this approach the Zhang-Rice band plays the role of the lower Hubbard band and an in-plane Cu band corresponds to the upper Hubbard band. The Hamiltonian contains a single kinetic-energy term proportional to the nearest-neighbor hopping amplitude t, in addition to the Hubbard U term

$$H = -t \sum_{<ij>,\sigma} (c^\dagger_{i\sigma} c_{j\sigma} + H.c.) + U \sum_i n_{i\uparrow} n_{i\downarrow} \qquad (2.3)$$

Here $c_{i\sigma}^{\dagger}$ ($c_{i\sigma}$) creates (annihilates) an electron or hole on site i with spin σ, $< ij >$ pinpoints nearest-neighbor pairs and $n_{i\sigma} = c_{i\sigma}^{\dagger}c_{i\sigma}$ is the number operator.

The Hubbard model simplifies into the t-J model, by projecting out the doubly occupied states at large U. The outcome Hamiltonian is more commonly used in studying the strong coupling limit ($U \gg t$) at half filling (i.e. x=0, one electron per Cu site in a $3d_{x^2-y^2}$ orbital). It results

$$H = -t \sum_{<ij>,\sigma} (\tilde{c}_{i\sigma}^{\dagger}\tilde{c}_{j\sigma} + H.c.) + J \sum_{<ij>} \left(\mathbf{S}_i \cdot \mathbf{S}_j - \frac{n_i n_j}{4} \right) \qquad (2.4)$$

where the operator $\tilde{c}_{i\sigma} = c_{i\sigma}(1 - n_{i-\sigma})$ excludes double occupancy, $J = 4t^2/U$ is the antiferromagnetic exchange coupling constant and $\mathbf{S}_i$ is the spin operator.

Multi-hole doped compound   Away from half filling, the t-J model describes a so-called doped antiferromagnet, namely a system of interacting spins and mobile holes. The single-band approach is based on the Zhang-Rice singlet located in single clusters (i.e. a Cu atom surrounded by four oxygen atoms), which doesn't necessarily mean that the same physics applies on the 2D Cu-O planes. In fact band formation and doping could destroy the stability of the local singlets in favor of other spin states. Recently an experiment performed on Bi2212 has strengthen the foundations of this theoretical structures. In fact a direct observation of the Zhang-Rice singlet is reported [21], the measurement was performed both in normal state and in superconducting state. This evidence is far from trivial.

3. STATICAL OPTICAL PROPERTIES

In this chapter we introduce the equilibrium optical properties of cuprates. First we report the classical models used to describe interband and intraband transitions, i.e. the Lorentz and Drude models. Then we consider the *extended Drude model* that accounts for the equilibrium reflectivity of the high-Tc superconductors. Finally we report the reflectivity data of $Bi_2Sr_2Ca_{0.92}Y_{0.08}Cu_2O_{8+x}$ optimally doped (Y-Bi2212 OP) in the three phases (normal state, pseudogap and superconducting state). We perform the fit to the data, using the previously described models. We comment some interesting and peculiar features of this reflectivity spectra.

3.1 **Classical models**

The classical theory of absorption and dispersion of light is due mainly to Lorentz and Drude. The Lorentz model is applicable to insulators, since it describes all direct interband transitions; i.e. all transitions for which the final state of an electron lies in a different band but with no change in **k**-vector in the reduced zone scheme.

The Drude model mimic the behavior of free-electron in metals, describing the intraband transitions, i.e. all the transitions within the same band which involve a change in the **k**-vector in the reduced zone scheme.

3.1.1 **Lorentz model**

Let us consider an atom with electrons bound to the nucleus in the same way as a small mass can be bound to a large mass by a spring: this is the Lorentz model. The motion of an electron bound to the nucleus is described by [1]

$$m\frac{d^2\mathbf{r}}{dt^2} + m\Gamma\frac{d\mathbf{r}}{dt} + m{\omega_0}^2\mathbf{r} = -e\mathbf{E}_{loc} \qquad (3.1)$$

where m is the electronic mass and e is the magnitude of electronic charge.

The field $\mathbf{E}_{loc}$ is the local electric field acting on the electron as a driving force and it is due to a light wave incident on the atom. The term $m\Gamma d\mathbf{r}/dt$ represents viscous damping and represents an energy loss mechanism.

---

[1]Bold letters represent vectors

For a free atom the actual loss mechanism is the radiation damping, while in a solid the radiation damping is related to various scattering mechanisms. The rate of these processes is Γ, so we can pinpoint the mean free time between electronic collisions with $\tau = 1/\Gamma$. The term $m\omega_0{}^2\mathbf{r}$ is a Hooke's law restoring force.

In the context of a classical model, there are two approximations in eq. (3.1). The nucleus is assumed to have an infinite mass, otherwise the reduced mass should have been used. We also have neglected the small Lorentz force $F = -e\mathbf{v}\times\mathbf{B}/c$ arising from the interaction of the electron with the magnetic field of the light wave. It is negligible because the velocity of the electron is small compared with c.

The local field can be assumed to vary in time as $e^{-i\omega t}$; thus the solution of eq. (3.1) is

$$\mathbf{r} = \frac{-e\mathbf{E}_{loc}/m}{(\omega_0{}^2 - \omega^2) - i\Gamma\omega} \tag{3.2}$$

and the induced dipole moment is

$$\mathbf{p} = -e\mathbf{r} = \frac{e^2\mathbf{E}_{loc}}{m}\frac{1}{(\omega_0{}^2 - \omega^2) - i\Gamma\omega} \tag{3.3}$$

We now assume that the displacement r is sufficiently small that a linear relationship exists between $\mathbf{p}$ and $\mathbf{E}_{loc}$, namely

$$\mathbf{p} = \alpha(\omega)\mathbf{E}_{loc} \tag{3.4}$$

where $\alpha(\omega)$ is the frequency dependent atomic polarizability. From eqs. (3.3) and (3.4), the polarizability for a one-electron atom is

$$\alpha(\omega) = \frac{e^2}{m} \frac{1}{(\omega_0{}^2 - \omega^2) - i\Gamma\omega} \qquad (3.5)$$

The polarizability is complex because of the damping term. As a result, the polarization differs in phase from the local field at all frequencies.

If there are N atoms per unit volume, the macroscopic polarization is

$$\mathbf{P} = N < \mathbf{p} > = N\alpha < \mathbf{E}_{loc} > = \chi_e \mathbf{E} \qquad (3.6)$$

where χ_e is the electric susceptibility. We made another assumption by considering $< \mathbf{E}_{loc} > = \mathbf{E}$; this equality is far from obvious. [2]

We are now ready to get an expression for the dielectric function in terms of the atomic polarizability; α is a complex quantity due to the presence of the energy loss mechanism term. This means that the fields $\mathbf{E}$, $\mathbf{P}$, and $\mathbf{D}$ are not in phase.

Let us define the complex displacement $\mathbf{D}$ such that

$$\mathbf{D} = \epsilon\mathbf{E} = \mathbf{E} + 4\pi\mathbf{P} \qquad (3.7)$$

---

[2]The equality holds only for metals, so strictly speaking it shouldn't be used in the Lorentz model. A satisfactory discussion can be found in [8].

From eqs. (3.6) and (3.7) we get

$$\epsilon = 1 + 4\pi N \alpha \tag{3.8}$$

using eq. (3.5) this becomes

$$\epsilon = 1 + \frac{4\pi N e^2}{m} \frac{1}{(\omega_0{}^2 - \omega^2) - i\Gamma\omega} \tag{3.9}$$

We can evaluate the real and complex part of the dielectric function

$$\epsilon_1 = 1 + \frac{4\pi N e^2}{m} \frac{(\omega_0{}^2 - \omega^2)}{(\omega_0{}^2 - \omega^2)^2 + \Gamma^2\omega^2} \tag{3.10}$$

$$\epsilon_2 = \frac{4\pi N e^2}{m} \frac{\Gamma\omega}{(\omega_0{}^2 - \omega^2)^2 + \Gamma^2\omega^2} \tag{3.11}$$

If we consider classical atoms with more than one electron, we can extend the previous results. Let N_j be the density of electrons bound with resonance frequency ω_j. Hence

$$\epsilon = 1 + \frac{4\pi N e^2}{m} \sum_{J} \frac{N_j}{(\omega_j{}^2 - \omega^2)^2 - i\Gamma_j\omega^2} \tag{3.12}$$

$$\sum_{j} N_j = N \tag{3.13}$$

A corresponding quantum mechanical equation can be derived [8]. It can be written as

$$\epsilon = 1 + \frac{4\pi e^2}{m} \sum_J \frac{N f_j}{(\omega_j{}^2 - \omega^2)^2 - i\Gamma_j \omega^2} \tag{3.14}$$

Despite of the formal similarity between eqs. (3.12) and (3.14), the meanings of some corresponding terms are quite different. In eq. (3.12), ω_j is the resonance frequency of a bound electron, whereas in eq. (3.14), it is the transition frequency of an electron between two atomic states separated in energy by $\hbar\omega_j$. The parameter f_j, called the oscillator strenght, is a measure of the relative probability of a quantum mechanical transition. For free atoms it satisfies the sum rule

$$\sum_j f_j = 1 \tag{3.15}$$

which is the quantum mechanical analog of eq. (3.13). All the optical constants can be derived from ϵ_1 and ϵ_2, as it is shown in appendix A; the most important relation is the connection between $\epsilon(\omega)$ and the refractive index $n(\omega)$, namely $n^2(\omega) = \epsilon(\omega)$ The reflectivity of solids at normal incidence is given by

$$R = \frac{(n_1 - 1)^2 + n_2{}^2}{(n_1 + 1)^2 + n_2{}^2} \tag{3.16}$$

where n_1 and n_2 are the real and imaginary part of the refractive index n. This result is also reported in appendix A.

Let us define another important quantity: the frequency at which $\epsilon_1 = 0$ is called the *plasma frequency* (ω_p). From eq. (3.10), assuming $\omega \gg \omega_0 \gg \Gamma$, it follows straightforwardly that

$$\omega_p{}^2 = \frac{4\pi N e^2}{m} \tag{3.17}$$

The Lorentz model is a highly idealized description of the behavior of an insulator.The optical response of real materials can be reproduced with a collection of Lorentz oscillators with different frequencies.

Finally it is worth to mention the *global oscillator strength sum rule* which is

$$\int_0^\infty \omega \epsilon_2(\omega) d\omega = \frac{1}{2} \pi \omega_p^2 \tag{3.18}$$

the evaluation of this integral is reported in appendix A. Let us show the physical origin of this sum rule: the rate of energy absorption ($\tilde{E}$) per unit volume from an electric field is

$$\frac{d\tilde{E}}{dt} = Re\left(\mathbf{E} \cdot \frac{\partial}{\partial t}\mathbf{D}\right) = Re\left[E \cdot (\epsilon_1 + i\epsilon_2)\frac{\partial}{\partial t}\mathbf{E}\right] \tag{3.19}$$

The field $\mathbf{E}$ has a time dependence $e^{-i\omega t}$, so it follows that

$$\frac{d\tilde{E}}{dt} = \omega\epsilon_2|\mathbf{E}|^2 \qquad (3.20)$$

Thus the integral

$$\int_0^\infty \omega\epsilon_2(\omega)d\omega \qquad (3.21)$$

is a measure of the energy absorption for all frequencies. This quantity is proportional to the ratio n/m (number of electrons versus the electronic bare mass) which is contained in the plasma frequency.

The sum rule can be expressed in terms of optical conductivity, by making use of the relation (A.10) we get

$$\int_0^\infty 4\pi\sigma_1(\omega)d\omega \qquad (3.22)$$

so

$$\int_0^\infty \sigma_1(\omega)d\omega = \frac{\omega_p^2}{8} \qquad (3.23)$$

Usually a partial sum rule is considered, because in experiments the conductivity is measured up to a certain frequency cutoff (ω_c). So we define the following quantity

$$W = \int_0^{\omega_c} \sigma_1(\omega)d\omega \qquad (3.24)$$

which is called *spectral weight*. This sum rule no longer depends on the total number of the electrons, because of the presence of the cutoff, but it is proportional to an effective number of electrons.

3.1.2 Drude Model

The Drude model is directly obtained from the Lorentz model by equating the restoring force to zero; in fact the conduction electrons of a metal can be considered free. From eqs. (3.10) and (3.11), assuming $\omega_0 = 0$ we obtain

$$\epsilon_1 = 1 - \frac{4\pi N e^2}{m} \frac{1}{\omega^2 + \Gamma^2} \qquad (3.25)$$

$$\epsilon_2 = \frac{4\pi N e^2}{m} \frac{\Gamma}{\omega(\omega^2 + \Gamma^2)} \qquad (3.26)$$

The origin of the viscous damping term for a free-electron metal is the ordinary scattering of electrons. The damping coefficient is related to the mean free time between collisions by $\Gamma = 1/\tau$, as already mentioned in the previous subsection. In general the value of τ is dependent on the temperature, but in the Drude picture it is frequency independent. This is a major and important feature of the Drude model.

We can write the dielectric function (real and imaginary part) using eqs.
(3.25), (3.26) and (3.17); thus we obtain

$$\epsilon_1 = 1 - \frac{\omega_p^2 \tau^2}{(1 + \omega^2 \tau^2)} \tag{3.27}$$

$$\epsilon_2 = \frac{\omega_p^2 \tau}{\omega(1 + \omega^2 \tau^2)} \tag{3.28}$$

The same result can be expressed in terms of optical conductivity $\sigma(\omega)$,
exploiting the eq. (A.8):

$$\sigma(\omega) = \frac{1}{4\pi} \frac{\omega_p^2}{1/\tau - i\omega} \tag{3.29}$$

3.2 **Extended Drude Model**

In the previous section of this chapter the two classical models have been reported, with the purpose of describing optical spectra of high Tc superconductors.

In common metals and insulators an optical conductivity composed by a Drude term and a set of Lorentz oscillators well fits the experimental optical data (for example reflectivity):

$$4\pi\sigma(\omega) = \frac{\omega_{pD}^2}{1/\tau_D - i\omega} + \frac{\sum_j \omega_{pj}^2 \omega}{i(\omega_j^2 - \omega^2) + \omega/\tau_j} \qquad (3.30)$$

where the subscript D and j are referred to the Drude term and to a single Lorentz oscillator among the whole set.

For high-T$_c$ superconductors the fit performed with eq. (3.30) doesn't account for the spectral features of the data, particularly in the infrared part of the spectrum (i.e. intraband transitions).

The reason lies on the physical assumptions the Drude model is based on: it gives a picture of the optical behavior typical of a free-electron metal. In this work we have studied the class of high-T$_c$ superconductors characterized by one or more copper-oxygen layers in the unit cell. These systems are called *cuprates*, they are strongly correlated systems; besides the interactions among electrons, a significant electron-boson interaction also occurs. These features are not described by the Drude model.

In this context the need for a more suitable model arises: the *extended Drude model*, which has been first employed to analyze the infrared conductivity of metals with a strong electron-phonon interaction in the limit of $T \to 0$ [11] and at finite T [12]. This formalism has been extensively applied to elemental metals, transition-metal compounds, heavy-fermion systems and the high T_c cuprates.

The basic idea deals with the mean free time between collisions (τ). As explained in the subsection (3.1.2) this parameter is independent of frequency in the Drude model. In the extended Drude model the electron-boson interaction is taken into account by assuming τ complex and frequency-dependent function: $1/\tau = M(\omega) = M'(\omega) + iM''(\omega)$, where $M(\omega)$ is called the *memory function* (or *optical self energy* [14]), which is

$$M(\omega, T) = \frac{1}{\tau(\omega, T)} - i\omega\lambda(\omega, T) \tag{3.31}$$

The complex conductivity can be expressed in terms of this function, so that

$$\sigma(\omega, T) = \frac{1}{4\pi} \frac{\omega_p{}^2}{M(\omega, T) - i\omega} \tag{3.32}$$

$$= \frac{1}{4\pi} \frac{\omega_p{}^2}{1/\tau(\omega, T) - i\omega[1 + \lambda(\omega, T)]} \tag{3.33}$$

The terms $1/\tau(\omega, T)$ and $1 + \lambda(\omega, T)$ describe the frequency dependent scattering rate and mass enhancement of electronic excitations due to many-body interactions. These two quantities are related by the Kramers Kronig transformation, as it is shown in [13].

The expression of the $1/\tau(\omega)$ is derived in [12] and it is

$$1/\tau(\omega) = 2\Gamma_i + \frac{1}{\omega} \int_0^\infty d\Omega \ \alpha^2(\Omega) F(\Omega) \left[2\omega \coth\left(\frac{\Omega}{2T}\right) \right.$$

$$\left. - (\omega + \Omega) \coth\left(\frac{\omega + \Omega}{2T}\right) + (\omega - \Omega) \coth\left(\frac{\omega - \Omega}{2T}\right) \right] \tag{3.34}$$

where $2\Gamma_i$ is the impurity contribution, whereas $\alpha^2(\Omega) F(\Omega)$ is the spectrum of the interacting bosons, as we will discuss in the following of this section.

Let us now spend a few words about the physics behind the memory function. According to many authors and experimental evidences in the superconducting cuprates the electrons are paired, like in the BCS materials, even if a general agreement on this issue has not been found yet. So far, the origin and the mechanism of the electron-pairing has not been determined. In some models [34] the aforementioned electron-boson coupling is considered as the glue of the pairing process. The glue is expressed through the spectral density of the bosons indicated as $\alpha^2(\Omega) F(\Omega)$ for phonons and $I^2(\Omega) \chi(\Omega)$ for spin-fluctuations. Strictly speaking $F(\Omega)$ is the phonon density of states (Ω is the phonon frequency) whereas $\alpha^2(\Omega)$ is a measure of the phonon frequency-dependent electron-phonon interaction.

Similar considerations hold for $I^2(\Omega)\chi(\Omega)$; we represent these two kinds of bosons as the general and dimensionless function $\Pi(\Omega)$.

An important consequence of the electron-boson coupling is that the energy (ξ) of the quasiparticles (QP) relative to the Fermi level is renormalized and the lifetime of QPs becomes limited by inelastic decay processes involving the emission of bosons.

The real and imaginary part of the optical self-energy are the the inverse lifetime and the term $\omega\lambda(\omega, T)$ (see eq. 3.33), which is a variation of the dispersion relation of the QPs.

The memory function is related to the single-particle self-energies by the formula

$$\frac{M(\omega)}{\omega} = \left[\int \frac{f(\xi) - f(\xi + \omega)}{\omega + \Sigma^*(\xi) - \Sigma(\xi + \omega)} \right]^{-1} + 1 \tag{3.35}$$

which is derived in [11]. The single particle self energy is expressed as the convolution of the *glue function* $\Pi(\Omega)$ with a kernel function $K(\xi, \Omega, T)$ which describes the thermal excitations of the glue and the electrons

$$\Sigma(\xi) = \int L(\xi, \Omega, T)\Pi(\Omega)d\Omega \tag{3.36}$$

The general expression for the Kernel function is

$$L(\xi, \Omega, T) = \int \left[\frac{n(\Omega) + f(\epsilon)}{\xi - \epsilon + \omega + i\delta} + \frac{n(\Omega) + 1 + f(\epsilon)}{\xi - \epsilon - \omega - i\delta} \right] d\epsilon \tag{3.37}$$

where $n(\Omega)$ and $f(\epsilon)$ are the Bose and Fermi-Dirac distribution functions respectively [11].

By performing the integration that involves the Fermi-Dirac distribution [30], the following explicit form for the kernel function can be obtained

$$L(\xi, \Omega) = -2\pi i \left[n(\Omega) + \frac{1}{2} \right] + \Psi \left(\frac{1}{2} + i \frac{\Omega - \xi}{2\pi T_e} \right) - \Psi \left(\frac{1}{2} - i \frac{\Omega + \xi}{2\pi T_e} \right) \quad (3.38)$$

where $\Psi(x, y)$ is the digamma function, which is the logarithmic derivative of the gamma function. This expression of the kernel function depends on both the electronic temperature $T_e(t)$ and the bosonic temperature $T_b(t)$ through the Bose distribution $n(\Omega)$.

Suppose to apply an AC electric field on a cuprate: the effect of the coupling between the electrons and the bosonic excitations is revealed by a frequency dependent dissipation (i.e. $1/\tau(\omega)$). This phenomenon can be understood as arising from processes where a photon is absorbed by the simultaneous creation of an electron-hole pair and a boson. Hence the optical conductivity in the normal state is expressed by eq. (3.32).

The central assumption in eq. (3.35) is the validity of the Landau Fermi-liquid picture for the normal state. This analysis is therefore expected to work best on the overdoped side of the cuprate phase diagram, where the state of matter appears to become increasingly Fermi-liquid like.

In order to fit reflectivity data the memory function of the system under study must be known. This is the reason why we now report the glue functions for some cuprates, which we have used to fit the data (see the following subsection). These glue functions have been obtained by van Heumen [15],
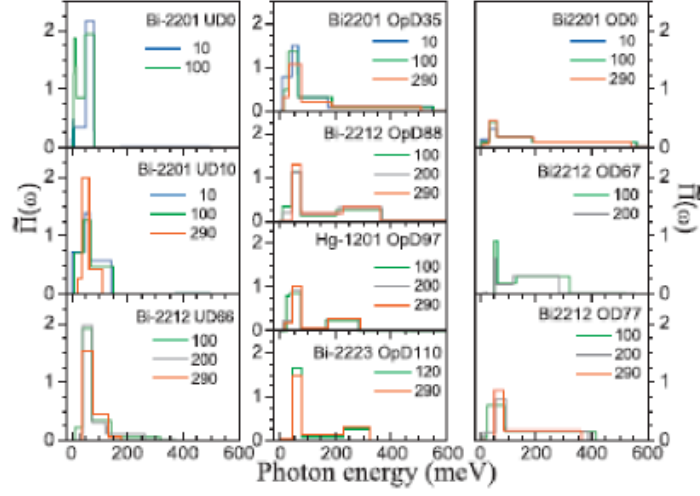
Figure 3.1: Electron-boson coupling function $\Pi(\Omega)$ for different cuprates at different doping levels and temperatures.

from previously published optical spectra, and are shown in figure (3.1).

From these graphs we can note that the bosons involved in the interaction with the electrons cannot be only phonons. In fact in the cuprates the phonon energies have an upper limit at about 100 meV; the glue functions have some spectral features also at higher energies, which means that other bosons (i.e. spin fluctuations) take part in the interaction.

Two main features can be observed from figure (3.1): a peak at $50-60$ meV and a broad continuum. There is a clear trend of a contraction of the continuum to lower energies when the carrier concentration is reduced. The most striking aspect of the peak at $50-60$ meV is the fact that its energy is basically independent of temperature and sample composition. Moreover, the intensity and the width are essentially temperature independent.

3.3 **Reflectivity Data**

We report the in-plane reflectivity data of Y-Bi2212 optimally doped (OP) in the three different phases: normal state (300 K), pseudogap (100 K) and superconducting state (20 K). These measurements have been performed by D. van der Marel's group by using different techniques, in order to cover all the spectral range between 50 cm^{-1} and 36000 cm^{-1} (in wavelength, from 200 μm to 280 nm). [3]

Data between 6000 and 36000 cm^{-1} have been collected with spectroscopic ellipsometry, whereas the infrared region of the spectrum was measured through reflectivity at normal incidence (as explained and reported in [6]). The complex dielectric function can be calculated from the reflectivity (eq. A.17). Thus we show the reflectivity and the dielectric functions of Y-Bi2212 OP in fig. (3.2) for the normal state, fig. (3.3) for the pseudogap and fig. (3.4) for the superconducting state.

In all these graphs the solid lines are the fit to the data, let us now explain how we fitted the data. The right approach to this analysis requires to consider separately the contributions of intraband and interband transitions. From the reported data we note that below 10000 cm^{-1} ($\sim$ 1.25 eV) the dielectric function is characterized by a Drude-like response. In the high energy region the interband transitions are overwhelming.

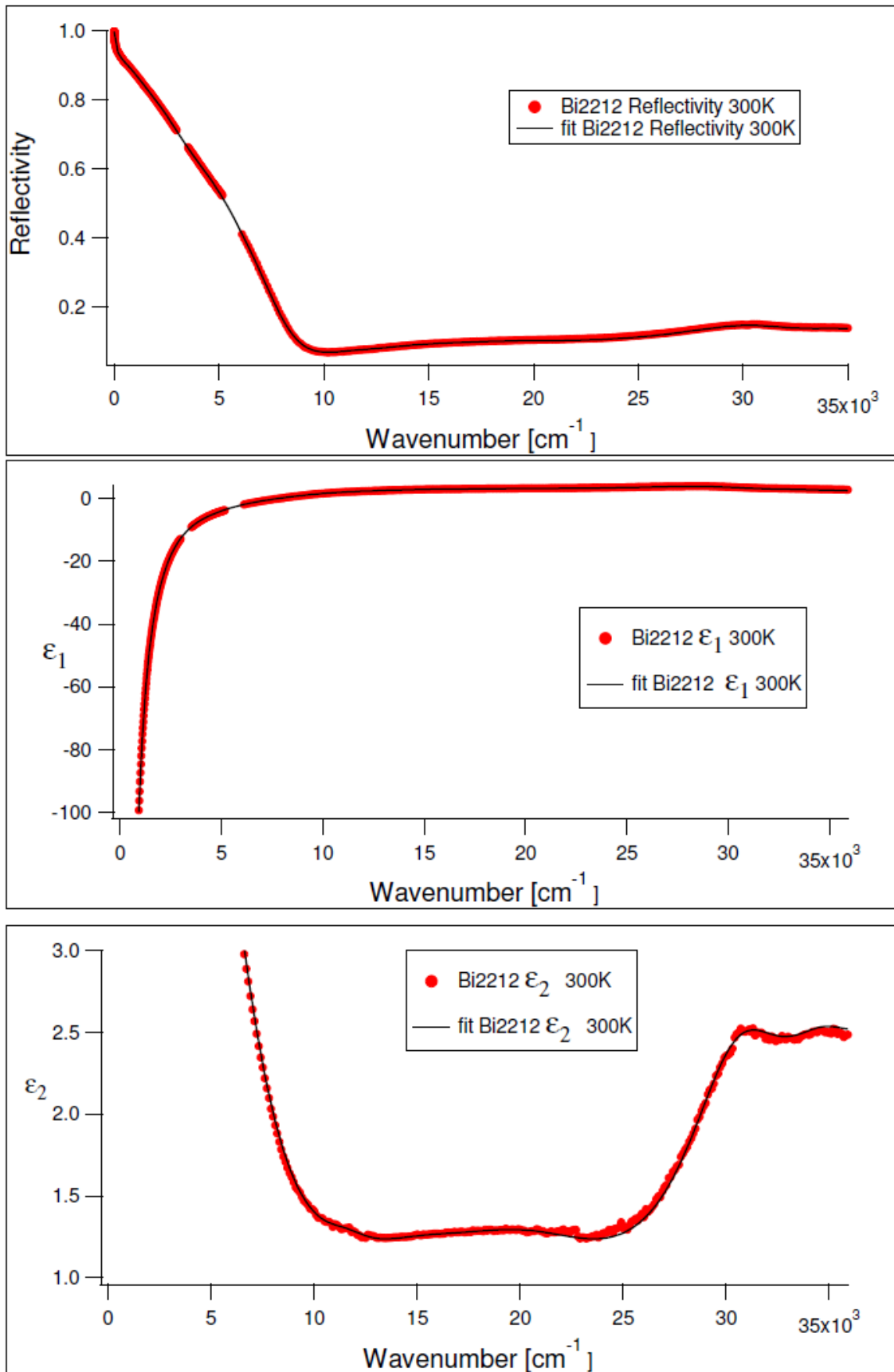[3]The conversion in energy is 8064 cm^{-1} = 1 eV

Figure 3.2: Y-Bi2212 Op 300 K: reflectivity, real and imaginary parts of the dielectric functions. Black lines are fit functions.
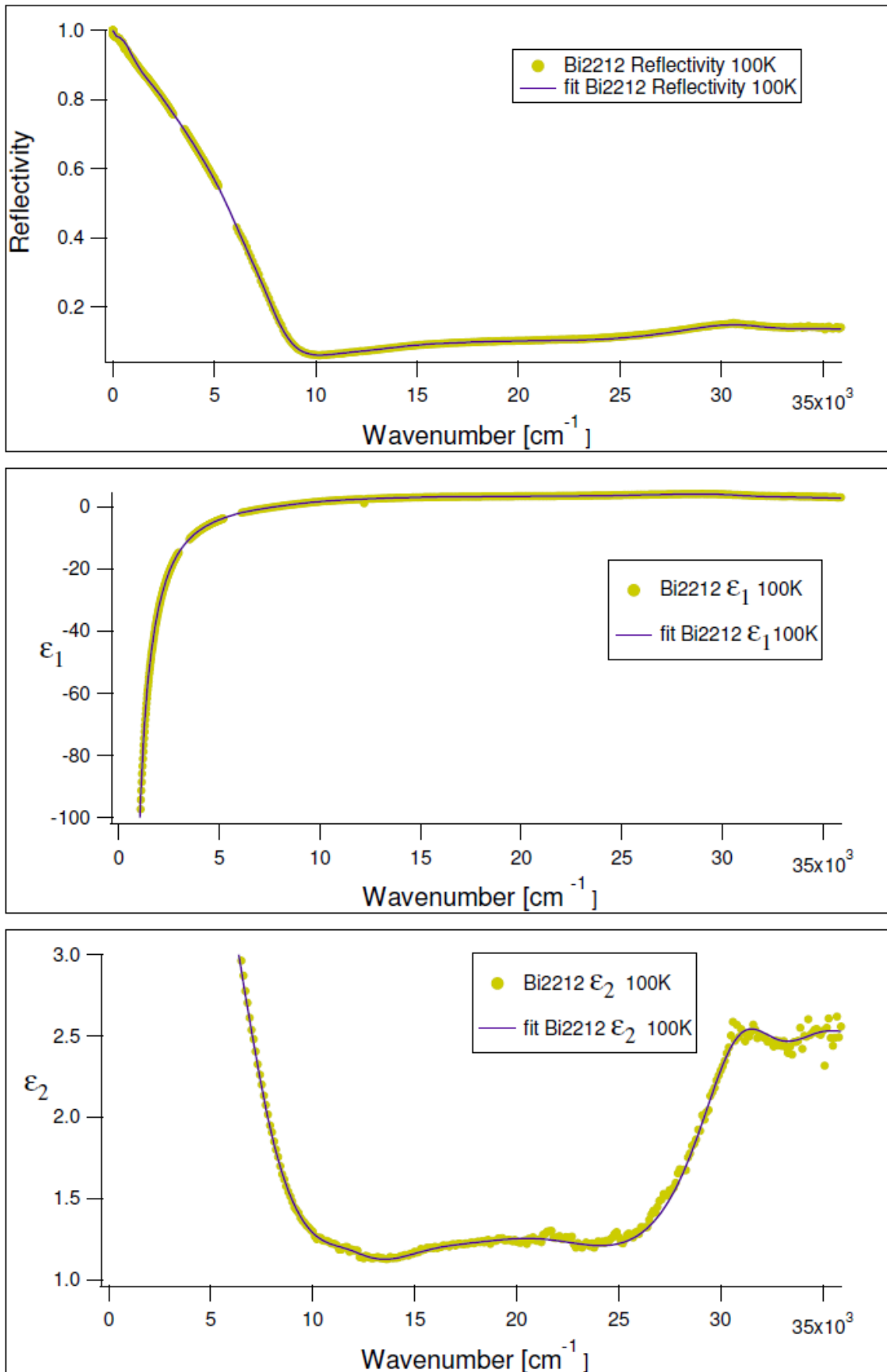
Figure 3.3: Y-Bi2212 Op 100 K: reflectivity, real and imaginary parts of the dielectric functions. Black lines are fit functions.
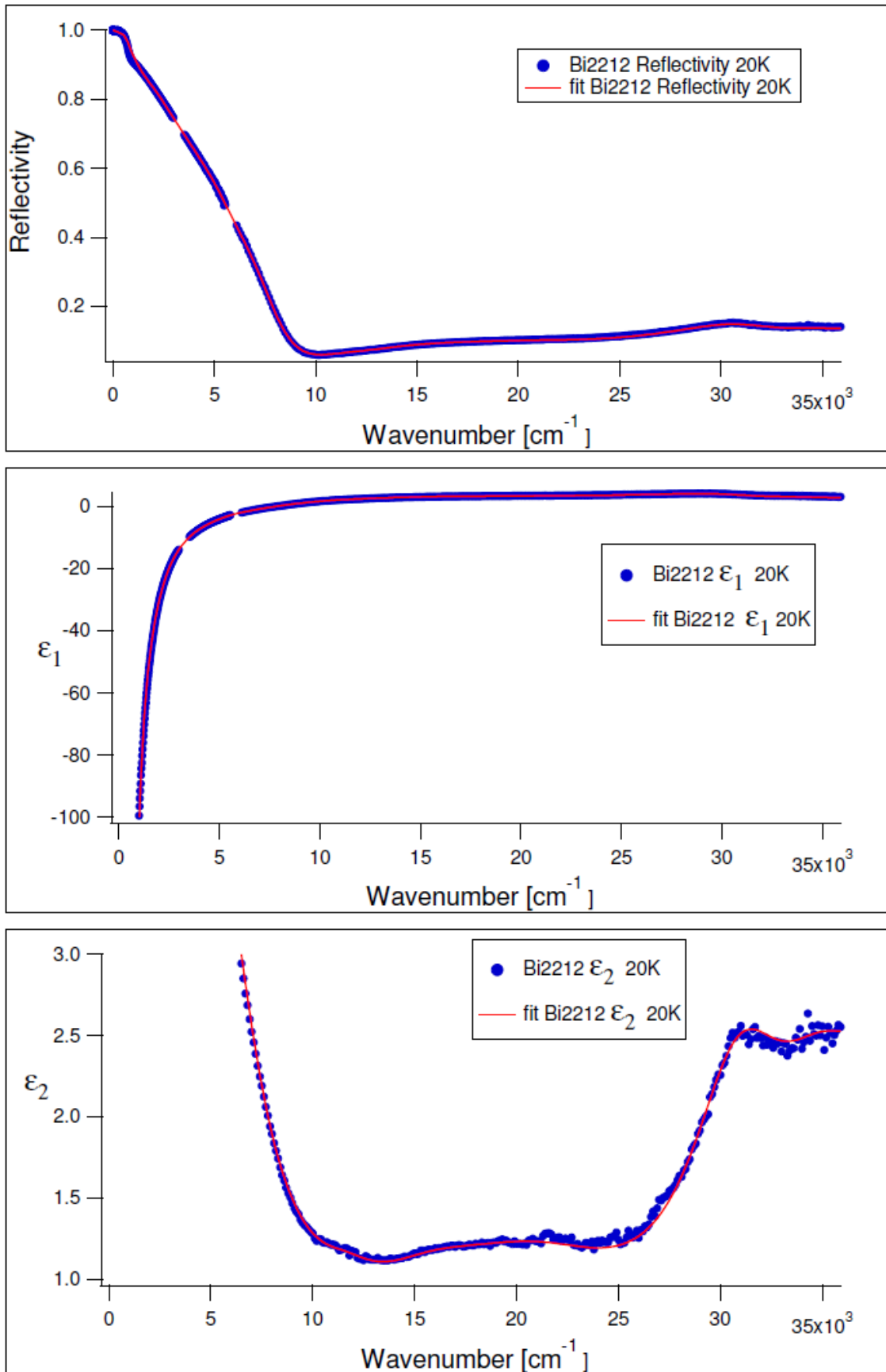
Figure 3.4: Y-Bi2212 Op 20 K: reflectivity, real and imaginary parts of the dielectric functions. Black lines are fit functions.

The dielectric function $\epsilon(\omega)$ has been fitted with a function of the same kind of eq. (3.30), with the main difference that we used the extended Drude model in order to describe the intraband transitions.

The electron-boson coupling term used is the glue function represented in fig. (3.1), which we described mathematically with sigmoid functions (P(x)), namely

$$P(x) = \frac{1}{1 + e^{-x}} \qquad (3.39)$$

Each sigmoid function involved in the fit procedure has three parameters: position, maximum value and width of the sigmoid.

The values of all the parameters used for the fit are reported in table (3.1); in this table we don't show the parameters of the sigmoid functions, because we obtained them from figure (3.1).

Provided the glue function, it is possible to fit the optical conductivity (and all the other optical functions) using eq. (3.32) and eq. (3.33). In the Kernel function, defined in eq. (3.37), we set $T_e = T_b = 20$ K (superconducting state measurements), 100 K (pseudogap measurement), 300 K (normal state measurement).

At the top of table (3.1) there are all the parameters that appear in the extended Drude model. The term ϵ_{inf} takes into account the dielectric function for an infinite value of the frequency; in principle (by looking at the formulas 3.13 and 3.14) it should be equal to 1. However we used a different value, because this allowed us to reduce the number of Lorentz oscillators: an increasing oscillators number would make ϵ_{inf} approach to 1.

The interband transitions were described by the eight Lorentz oscillators (see subsection (3.1.1)) reported in table (3.1); each of these contributions is characterized by three parameters: position (ω_0), plasma frequency (ω_p) and width (γ).

In figure (3.5) we have reported the data of the measurement in superconducting state with the fit. Besides the contributions to the dielectric function of some oscillators are shown, it is also clear that the intraband and interband transitions dominate the optical response in different spectral ranges, separated roughly at 10000 cm^{-1} (1.25 eV).

Looking at the table (3.1) we note that two oscillators are centered at 4234 and 6490 cm^{-1}; thus they lie in the intraband region of the spectrum.

These oscillators represent a spectral feature typical of the cuprates, called the *mid-infrared peak*. This structure appears in doped systems, whereas it is absent in undoped samples [16]. The mid-infrared peak has typical energy of 0.5 eV, which corresponds barely to 4000 cm^{-1}; this is roughly the spectral position where we used two oscillators.

Parameters	T=300 K	T=100 K	T=20 K
ϵ_{inf}	3	3	3
ω_p	17418	17392	16901
Γ_{imp}	53	155	625
T	20	100	290
ω_0	4234	4929	4264
ω_{p0}^2	10454991	13871222	22041800
γ_0	3535	4706	4069
ω_0	6490	6959	6789
ω_{p0}^2	11001998	6489852	8142014
γ_0	3519	2949	3925
ω_0	11800	11800	11650
ω_{p0}^2	5560610	7460610	5307060
γ_0	3644	3944	3500
ω_0	16163	16163	15409
ω_{p0}^2	40768500	41268500	45542000
γ_0	8304	8304	8905
ω_0	21947	21947	21300
ω_{p0}^2	225776000	230776025	223159025
γ_0	13998	13898	13898
ω_0	31057	31057	30756
ω_{p0}^2	288626121	288626121	320536896
γ_0	6191	6191	6908
ω_0	35146	35146	34946
ω_{p0}^2	217474009	217474009	214474009
γ_0	6396	6396	6396
ω_0	40421	40421	40421
ω_{p0}^2	750212100	750212100	756371984
γ_0	7518	7518	7518

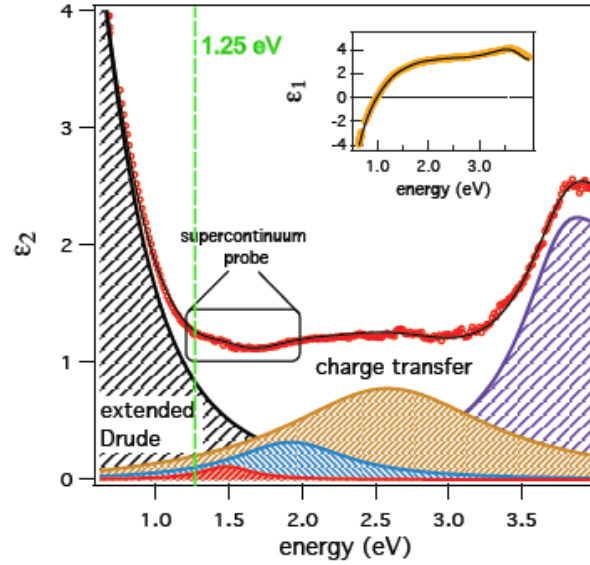Table 3.1: Fit Parameters: extended Drude model and Lorentz oscillators.

Figure 3.5: Dielectric function of optimally-doped Y-Bi2212: the in-plane dielectric function measured at T=20 K is shown. The black line is the fit to the data obtained by the sum of the extended Drude model and eight Lorentz oscillators. We put in evidence the edge ($\sim$ 1.25 eV) of the regions in which intraband ($E < 1.25$ eV) and interband ($E > 1.25$ eV) transitions dominate.

The physical process represented by the mid-IR peak is still debated. Many suggestions have been done [16] and in particular we mention the one reported in [17], according to which this spectral feature is the signature of the transition of the quasiparticles from the lower Hubbard band. This interpretation allows us to use Lorentz oscillators in order to fit the data.

The other oscillators represent different phenomena, in particular the first two (11800 and 16163 cm^{-1}, so 1.5 and 2 eV) are related to *charge-transfer* transitions. These are transitions of a hole from the Cu d orbital (in particular d$_{x^2-y^2}$) to the O 2p orbital, as it is represented in fig. (3.6).
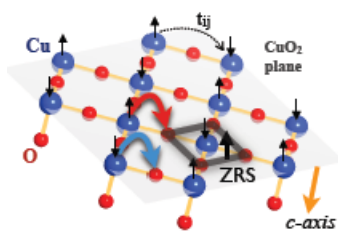
Figure 3.6: Representation of the in-plane charge-transfer transitions. The Zhang-Rice singlet is also shown.

The lowest energy process is expected to involve the so called *Zhang-Rice singlet*: it is a state in which a hole is shared by the four oxygen atoms that surround a copper. The hole's spin is coupled antiferromagnetically with the hole in the Cu d orbital. This singlet state represents the ground state of the undoped cuprates, when a single hole is added (as reported in [18] and [20]).

In fact the undoped parent compounds, as predicted by the Mott-Hubbard theory [19], have an insulating and antiferromagnetic ground state. This picture accounts for the AF phase appearing in the phase diagram (fig. 2.3) in correspondence of the zero-doping regime. Doping the system is equivalent (as explained in [20] and [19]) to adding holes in the cuprates; these holes are energetically more favoured to be shared by the oxygen atoms (as demonstrated by Zhang and Rice in [18]) than being localized on the cooper site (due to the strong Coulomb repulsion). This explains the antiferromagnetic coupling between the two holes' spins. This bound state can now hop from site to site: however this doesn't justify the conducting properties of the normal state doped cuprates. In fact the interactions among more singlets is not taken into account; besides when the system is doped with many holes (more than one) the ground state is unknown. The Zhang-Rice singlet has

been demonstrated to be the ground state only in case of single hole doping. The physics of the cuprates is more deeply analyzed in section (2.3).

The other higher energy oscillators that appear in the fit function are related to other transitions, in particular we mention the charge-transfer processes that involves different orbitals of Cu (not the $d_{x^2-y^2}$) and O. These transitions don't occur within a single Cu-O plaquette, but they concern further neighbor coppers (and the surrounding oxygens) and atoms out of plane.

4. DIFFERENTIAL FIT

This chapter is they keystone of the whole present work. It contains the reason why we decided to perform time-resolved reflectivity measurement in the infrared region of the spectrum.

4.1 Differential fit

In section (3.2) we described the extended Drude model, obtaining an expression for the optical conductivity (eq. 3.32). We used this result to fit the equilibrium reflectivity data, as reported in section (3.3). As explained in section (2.2) the aim of the present work is to study non-equilibrium dynamics in Y-Bi2212, so another fit procedure is required to fit the data. The measurement in fact deals with the reflectivity variation due to the pump pulse excitation $(\Delta R / R_{eq} = (R_{exc} - R_{eq})/R_{eq})$.

An important result obtained in the extended Drude model is expressed in eq. (3.35): the memory function (consequently all the optical functions) depends on both the electronic temperature T_e, via the Fermi-Dirac distri-

bution, and the bosonic temperature T_b, via the single-particle self-energy. In particular we recall eq. (3.37) which clearly states that there is a contribution of both T_e and T_b (through the Bose distribution $n(\Omega)$) to the Kernel function. Moreover it is worth to be stressed that the value of the two temperatures are disentangled. Provided the link between the Kernel function and the single-particle self energy (eq. 3.36), it follows that the memory function can be calculated considering electronic and bosonic temperatures different in values.

Thus it becomes possible to evaluate the variation of the dielectric function due to the pump-induced excitation

$$\delta\epsilon(\omega) = \epsilon_{exc}(T_e, T_b) - \epsilon_{eq} \tag{4.1}$$

The main subject of this work is the relaxation dynamics, due to the electronic thermalization with the bosonic heat bath. The dielectric function variation corresponding to this process can be fitted using eq. (4.1) setting a T_e value bigger than T_b. Our experimental measurement deals with reflectivity, which is obtained from the dielectric function by using eq. (A.17).

In figure (4.1) we report the calculated reflectivity variation of Y-Bi2212 optimally doped in the superconducting state (T=20 K). The green line was obtained raising the electronic temperature by $\Delta T_e = 20$ K. The blue line describes an increase of both the electronic and bosonic temperatures $\Delta T_e = \Delta T_b = 20$ K. From this graph it is clear that, in the visible region of the spectrum, the electronic thermalization dynamics is not detectable.
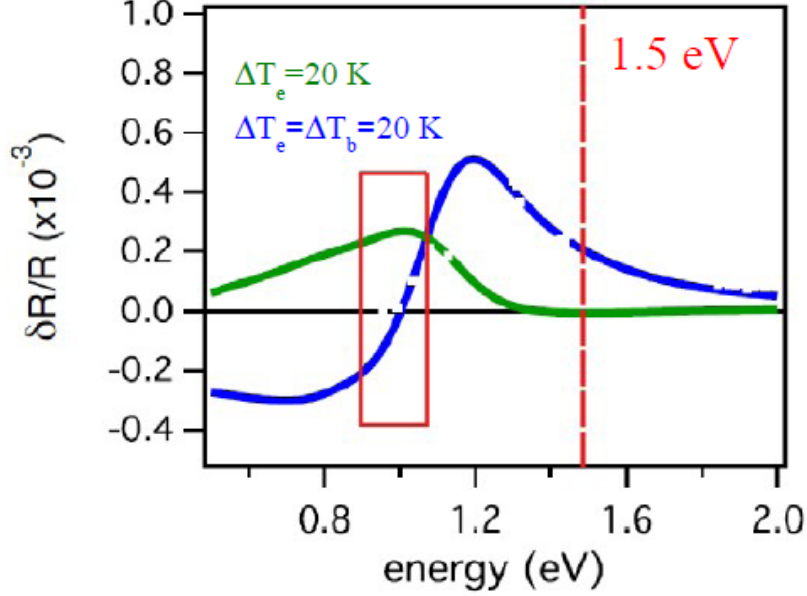
Figure 4.1: Calculated reflectivity variation for Y-Bi2212 OP in superconducting state. The energy value of 1.5 eV is put in evidence. The red box describes the energy range in which the electronic thermalization dynamics dominates.

In fact it is covered by the relaxation dynamics which involves the bosons: this means that the bottleneck occurs. All the experimental evidence about optical measurements reported in the literature, for example [39], are about single-wavelength experiments performed at 1.5 eV. So far the electronic thermalization dynamics in the superconducting state has not been observed in optical experiments yet. Otherwise other technique let to study the electron-boson coupling in the superconducting cuprates [28] [27].

The most interesting information in fig. (4.1) is that in a particular spectral region the electronic dynamics dominates. This region is the infrared one (enclosed by the red box in the figure); it means that in principle an optical experiment performed in this spectral range should be able to detect

the electronic dynamics. Thanks to the time resolution of the laser pulses, it is possible to study the sub-picosecond processes in the superconducting state.

Hence the brand new thing presented in this work is a time and spectral resolved pump and probe measurement, performed on Y-Bi2212 in the superconducting state. The spectral region analyzed is 1200-2400 nm (barely $0.5 - 1$ eV), which covers the red box zone in figure (4.1).

The direct observation of the electronic thermalization dynamics allows us to provide an estimation of the electron-phonon coupling constant, in the superconducting phase.

5. EXPERIMENTAL SET-UP

This chapter contains the description of the experimental set-up. This apparatus allowed us to perform pump and probe spectroscopy measurement in the infrared region of the spectrum. The main features of our set-up are the repetition rate of the laser system (250 kHz), which let us to work in the low fluence (less than 50 μJ/cm^2) regime avoiding undesired thermal heating effects, and the tunability of the probe beam, achieved by an Optical Parametric Amplifier (OPA) which can tune the output of the laser (800 nm) in the spectral range 1200-2400 nm.

First we introduce the pump and probe technique, then we describe all the devices that appear in the set-up in details, especially the laser system.

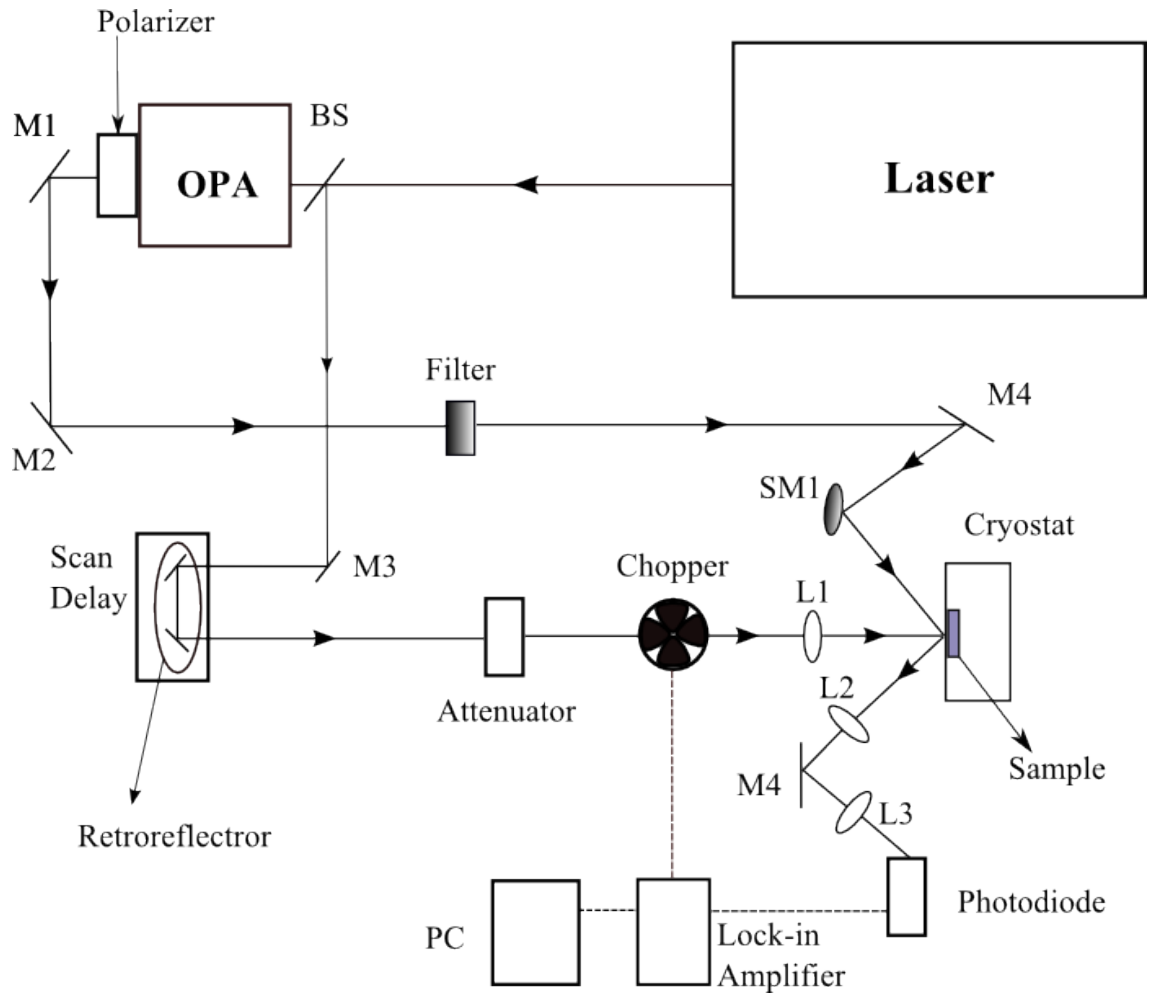We also report the characterization of the sample used in the experimental activity.

Figure 5.1: Set-up for the infrared measurement

5.1 Set-up and Pump and Probe technique

In this section we briefly introduce the set-up reported in fig. (5.1), a detailed description of all the devices and instruments that form the apparatus can be found in the following sections. Then we explain how the experimental technique works.

Finally some features of the acquisition system are reported.

Set-up   Let us now take a look at the set-up, briefly describing the optical path of the laser beam. The set-up realized to perform the measurements in the infrared part of the spectrum is schematically shown in figure (5.1). In this picture the box named *Laser* actually represents all the optical cavities forming the laser source (5.2).

The optical beam produced by the laser system is split into two beams by a beamsplitter (BS in the figure) 70-30: these are the pump (70 % of the laser output power) and the probe (30 % of the laser output power). The former is directed towards the Scan Delay, then it is reflected into the attenuator, which is a device composed by a rotatable half-wave plate and two mirrors at the Brewster angle. Finally the pump passes through the chopper and it is focused on the sample by the lens called $L1$ ($f = 40cm$) in figure (5.1).

To obtain the tunability of the probe wavelength, an Optical Parametric Amplifier is used. The probe beam enters the OPA, that allows us to obtain tunable coherent pulses in the spectral range of $(1200-2400)$ nm. The output of the OPA is attenuated by the use of a filter. Finally the probe is focused on the sample by the spherical mirror $SM1$ ($f = 30$ cm), the reflected beam is collected by the lens $L2$ ($f = 12.5$ mm) and then is focused by $L3$ ($f = 5$ cm) into a photodiode; this signal is acquired via the lock-in amplifier. The choice to focus the probe through a spherical mirror is due to the need to avoid the chromatic aberrations of standard lenses.

The Pump and Probe technique The goal of this work is to study the non equilibrium optical properties (i.e. reflectivity and transmission) of the high T_c superconductors with temporal resolution. In our set-up we measured the variation in the sample's reflectivity; the same technique can be used for the transmission measurements. The technique to achieve this goal is the *pump and probe* technique; it gives the temporal resolution to the measurement, due to the time structure od the laser pulses, that is not provided by the equilibrium measurements.

The pulses have femtosecond duration, this means that it is possible to study the dynamics of the optical response out of equilibrium with sub-picosecond time resolution. In addition the Optical Parametric Amplifier (OPA, see section 5.2.5) in our set-up allowed us to perform the pump and probe technique over a broad spectral range (1200-2400 nm, so 0.5-1 eV); this feature makes our measurement a time-resolved spectroscopy. Another characteristic of this technique is the high sensitivity: in fact it allows the detection of very small relative signals (on the order of 10^{-4}).

In our experimental activity we measured the normalized variation of reflectivity, in order to compensate for intensity fluctuations. So we detected the quantity

$$\Delta R(\tau) = \frac{R_{exc}(\tau) - R_{eq}}{c} \qquad (5.1)$$

where τ is the delay between the two optical beams involved in the measurement, $R_{excited}(\tau)$ is the reflectivity of the pump excited sample and R_{eq} is the reflectivity in the equilibrium state.
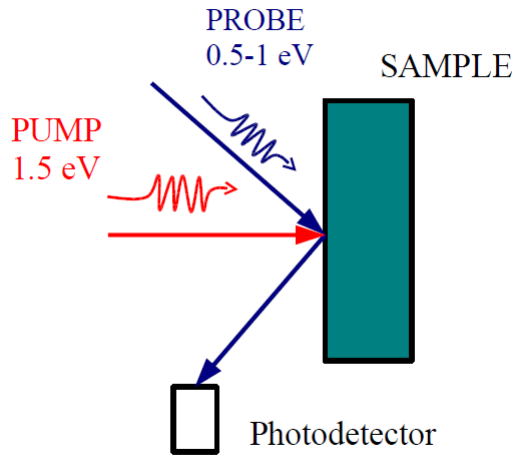
Figure 5.2: Schematic representation of the pump and probe experiment; the temporal delay between the two beams is set and controlled by the Scan Delay.

Let us describe how this measurement technique work. The first step of the pump and probe technique consists in splitting the output of the laser system into two beams, which we define *pump* and *probe*. The former excites the sample, while the latter (as its name suggests) probes the variation of the optical response of the system, induced by the pump.

These two beams cover two different optical paths, which must be of the same length because they have to fulfill the coincidence (spatial and temporal) condition on the sample (as shown in fig. 5.2).

The temporal coincidence is required because laser pulses has a time-structure in the femtosecond regime; if this condition is not satisfied the probe cannot detect the effects in the optical properties due to the presence of the pump.

Pump and probe are staggered in time by the use of the Scan Delay (see figure 5.1): it is a motorized device that contains a system of mirrors (called

the retroreflector), mounted on a sledge, placed in the optical path of the pump. The Scan Delay is described in subsection (5.5).

The spatial coincidence is required to probe the same area of the sample perturbed by the pump: this requirement force a condition on the beams' spot sizes: to probe a uniformly excited zone of the superconductor, the spot size of the probe must be smaller than the pump's one. The lens L1 ($f = 40$ cm) focuses the pump beam (see fig. 5.1) to a spot whose diameter is $D = (88.8 \pm 2.1)$ μm; the probe is focused on the sample by the spherical mirror SM1 ($f = 30$ cm) with a diameter value of $D = (30.3 \pm 1.7)$ μm. The measurement of the spot sizes is reported in section (5.2.6).

Another important constraint is the intensity of the probe, that must be limited to avoid strong excitation of the system. So the probe has to be a low fluence (< 50 μJ/cm^2) beam, fluence is defined in section (5.2.6). For this reason we alternatively used two different filters with optical density (OD) 2 (i.e. Transmittance= 10^{-2}, so 1 %) and 3 (i.e. Transmittance= 10^{-3}, so 0.1 %), as shown in fig. (5.1) in order to attenuate the probe intensity.

The signal to detect is very low, so we want to exclude any other contribution to the signal, except from the pump induced reflectivity change. We used pump and probe beams with orthogonal polarization to avoid possible interference effect; the pump is s-polarized while the probe is p-polarized. An interesting feature of our set-up is the possibility to change the pump's fluence, so that perturbations at different intensities can be induced in the sample. This is provided by the attenuator, which is a system composed by a rotatable half-wave plate and two mirrors at the Brewster angle, which select the vertical polarization (the attenuator is described in subsection 5.3).

This device allows us to perform time-resolved measurements in different regimes:

- in the high fluence regime (> 50 μJ/cm^2) the pump excitation impulsively destroy the superconductivity.

- in the low fluence regime (< 50 μJ/cm^2) the pump weakly perturbs the superconducting condensate.

In the present work we are going to report measurements performed in the low-fluence regime.

The source is a laser system (described in section 5.2) eith 250 kHz repetition rate. The value is the optimal trade-off between high repetition rate sources (for example 80 MHz which is typical of an oscillator, Mira Seed in our set-up) that are suitable for the low-fluence measurements but destroy the superconductivity by thermal heating (i.e. high mean power), and low repetition rate (on the order of 1 kHz) sources, that work at very high fluences, impulsively destroying the superconductivity. The 250 kHz source allows us to work in the low fluence regime, while keeping a high signal without any average heating effect, in fact the laser power on the sample was $P = 7.98$ mW. Comparing our source with an oscillator, despite the reduced repetition rate, the energy content of each single pulse is not strongly suppressed: the pulse intensity is 20 GW/cm^2.

Acquisition system   The signal variation induced by the pump is extremely small, so the acquisition is a critical step. To overcome this hardness we relied on the lock-in technique. The reflected probe is collected by two lenses into a photodiode, that is linked to the lock-in amplifier. In this scheme the pump is modulated by the chopper which supplies the frequency and phase reference to the lock-in amplifier. This instrument selects and acquires only the component of the reflected probe modulated at the reference frequency (13 kHz). This procedure allows us to acquire the pump induced variation of the reflectivity, without the noise related to other frequencies.

The choice of the chopper's frequency has some constraints: it has to be the highest possible value, in order to suppress the $1/f$ noise, but lower than the laser repetition rate because, in that case, only a few pulses would pass through the open window of the chopper. Considering 250 kHz as the repetition rate and 13 kHz as the chopper's frequency, we get $250 : 13 : 2 \sim 10$ pulses per each open window of the chopper. The factor 2 takes into account the duty cycle ($50\,\% - 50\,\%$) of the chopper. Given also some considerations reported in section (5.4) it follows that the oprimal choice is 13 kHz.
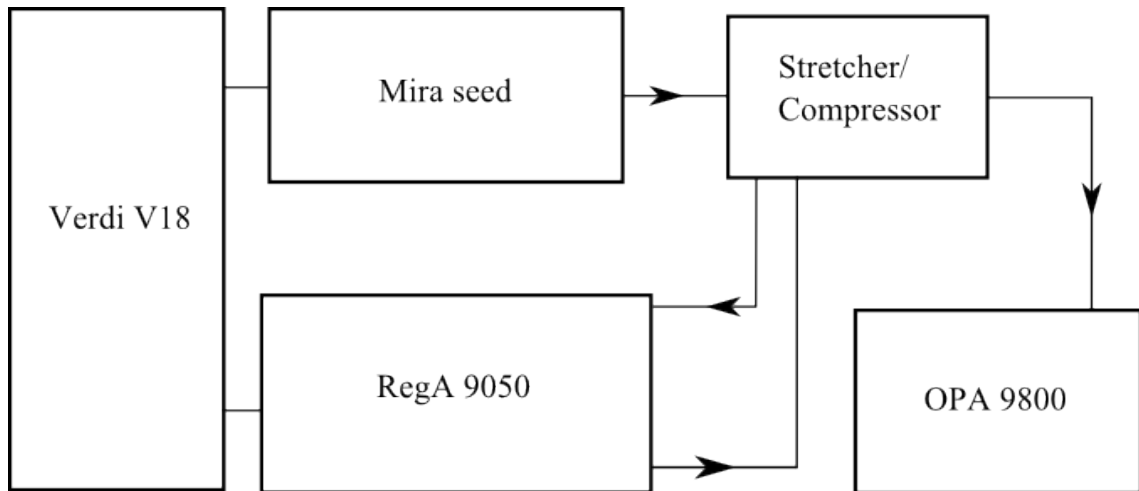
5.2 **Laser system**

Figure 5.3: Laser system

In this section we describe the details of the laser source, which is displayed in figure (5.3). It consists of:

- Coherent Verdi V-18 laser

- Coherent Mira Seed laser

- Coherent Stretcher/Compressor

- Coherent RegA 9050

- Coherent OPA 9850

5.2.1 **Verdi V-18**

In our set-up the Coherent Verdi V-18 is the optical pump for both the Mira Seed and the RegA. It is a compact solid-state diode-pumped, frequency doubled Nd:Vanadate (Nd:YVO$_4$) laser that provides continuum monochromatic green (532 nm) output, with 18 W of power output.

The Verdi V-18 laser consists of the laser head and power supply connected by an umbilical (i.e. a cylindrical pipe that contains fibers and cables): a chiller is used to cool down both the laser head and the power supply. Inside the umbilical there are fiber optics and electrical cables. The fiber optics transmit light from the diode bars in the power supply to the laser head, the electric cables provide control and monitoring signals between the laser head and the power supply.

The laser head contains the following optical elements (hermetically sealed in the head):

- Vanadate as the gain medium

- LBO non-linear crystal (for Second Harmonic Generation)

- Optical diode

- Astigmatic compensator and four cavity mirrors

- An etalon as the single-frequency optic

The temperature of the Vanadate and etalon are controlled by thermo-electric coolers (TECs), which are capable of heating or cooling the optical element.

The temperature of the lithium triborate (LBO non-linear crystal) is controlled by a resistive heater: this crystal is held at approximately 148° C. To prevent rapid change of temperature that may cause LBO crystal damage during warm-up, a CPU in the power supply regulates a slow ramp-up to operating temperature. In case of loss of AC power the laser undergoes a battery powered, CPU-controlled, cool-down process that lowers the LBO's temperature gradually to room temperature. There is one important feature to notice: the LBO is a Type I non critically phase matched crystal, which means that a little change of the temperature's value implies a dramatic collapse in the Second Harmonic conversion efficiency. Actually a 0.5° C variation cause an efficiency's decrease of nearly 50 %; this the reason why temperature control of the LBO is a key aspect to make Verdi work properly. In fact the phase matching condition is achieved because the birifrangent properties of the LBO are temperature-sensitive; so the value of 148° C is the proper one to obtain phase matching at the wavelength of the two pump diodes (located in the power supply).

Accumulated heat in the laser head is dissipated by a water-cooled heat sink mounted on the laser head baseplate. Baseplate temperature is monitored by the CPU, which will shut the system down if the laser head temperature reaches 55° C.

The laser head utilizes a Neodymium Vanadate (Nd:YVO$_4$) crystal as active medium with the pump power provided by fiber delivery; this medium is a homogeneously broadened system, so the Verdi tends to naturally run single frequency, with the etalon reinforcing this behaviour.

A photodiode in the laser head monitors the laser output; it allows the CPU to control the Verdi output power by adjusting the diode pump power to the Vanadate, in order to get the power value requested by the user from the power supply front panel.

The pump diodes' temperature is held constant by the TECs. Excess heat is dissipated by forced air cooling through heat sinks, which are located within the power supply.

5.2.2 Mira Seed

The Coherent Mira Seed Laser is a Titanium:Sapphire (Ti:Sapphire, Al_2O_3 doped with Ti_2O_3) oscillator, pumped by the Verdi. It is a mode-locked laser that produces ultra short, wide bandwidth, femtosecond pulses at a repetition rate of 76 MHz. We used the laser at the wavelength of 800 nm, which gives the best results in terms of stability and pulse quality (bandwidth and pulse duration): in fact the pulse out of Mira Seed has 30 nm of bandwith and 120 fs of duration. It is tunable from 760 to 840 nm, the tuning capability results in an increase of the pulse duration and a reduction of the bandwidth. The output beam has horizontal polarization (so p-polarization) and the spatial mode is the TEM_{00}.

The technique used to mode-lock the Mira Seed Laser is called *Kerr Lens Mode-Locking* (KLM). The optical cavity is designed specifically to exploit changes in the spatial profile of the beam (i.e. self-focusing) due to the optical Kerr effect produced in the Ti:Sa crystal, that is also the active medium of the laser. This mechanism results in higher round-trip gain in the mode-locked than in the continuous wave (CW) operation; it can easily be shown

[4] that the ratio of the pulse peak power in the mode-locked regime versus the modes' random phase relation regime reaches values of $10^3 - 10^4$ in solid state lasers. In addition an aperture is placed at a location where the mode-locked beam diameter is smaller to produce minimal round trip losses. The negative group velocity dispersion (GVD) accomplished by the optical media in the cavity results in reduced third-order dispersion with bandwidth grater than 50 nm.

5.2.3 Stretcher/Compressor

The Coherent Stretcher/Compressor is a device capable of stretching in time the pulse out of Mira Seed and then of re-compressing it. The main idea is to stretch in time the Mira's pulse, amplifying it up to saturation in RegA, then recompress the pulse by a second pass in the Stretcher/Compressor as it is shown in figure (5.3). Finally we get a pulse of $\sim$ 50 fs duration and high peak power ($\sim$ 20 GW/cm^2).
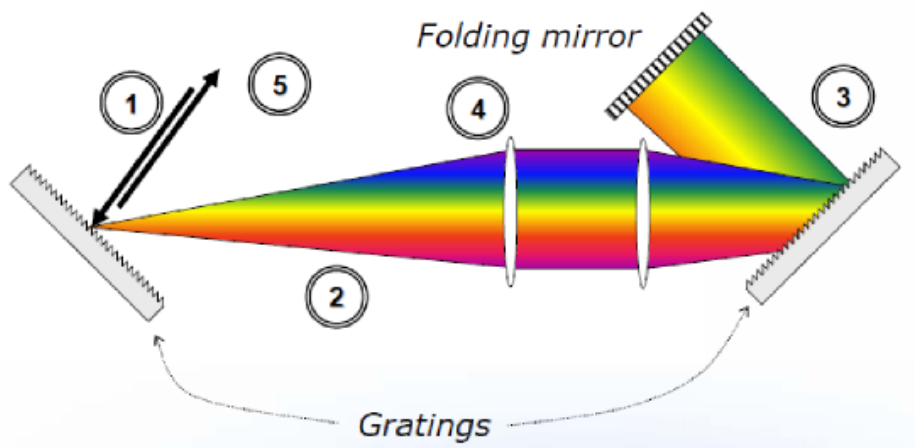

Figure 5.4: Stretching process of the pulse: 1) Input; 2) Positive dispersion; 3) Collimation of the beam; 4) Eliminating spatial chirp; 5) Output.
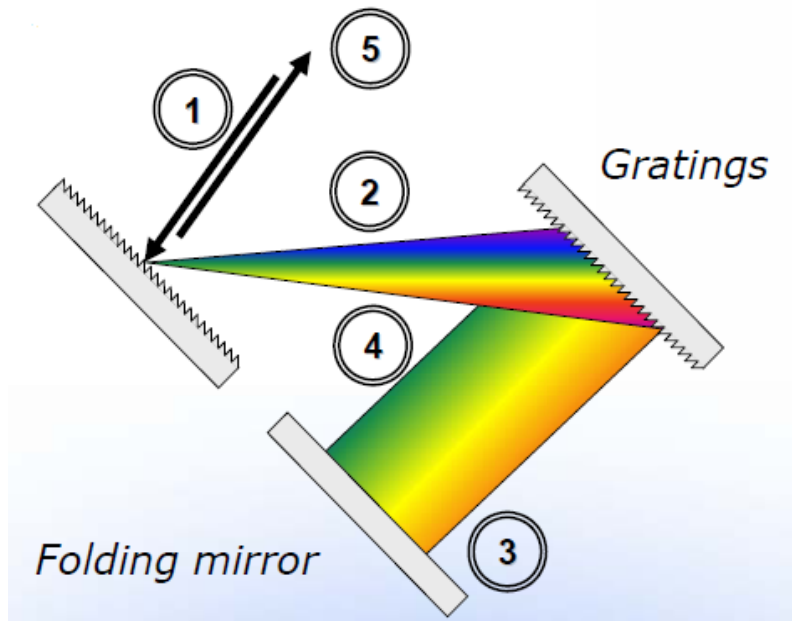
Figure 5.5: Compression of the pulse temporal width: 1) Input; 2) Negative dispersion; 3) Collimation of the beam; 4) Eliminating spatial chirp; 5) Output.

The stretching and compression operations occur by the use of diffraction gratings, as described in figure (5.4) and (5.5). Let us take a closer look to these two stages: the input of the Stretcher is the Mira Seed's short pulse, which has no chirp (it is approximately transform limited). The set of lenses shown in figure (5.4) induces positive dispersion, so the pulse acquires spatial and time chirps. The beam is then collimated and the spatial chirp is compensated by the system of lenses (fig. 5.4 stage (4)); finally the output pulse has only a temporal chirp (long pulse). Let us suppose to perform the compression operation on a transform limited (no chirp) pulse: the situation is pretty similar to the stretcher's one, with the basic difference that compression induces a negative chirp in the pulse. This two processes (i.e. stretching and compression) have to be balanced in order to obtain a trans-

form limited pulse, but there is also another contribution that must be taken into account. The pulse is amplified by RegA (after the stretching stage and before the compression one), that adds another contribution to the pulse's dispersion (actually a positive contribution) dependent on the thickness of the optical media in RegA and on the number of round trips.

To compress the pulse successfully it is necessary to balance the total dispersion of the pulse to second order (group velocity dispersion, GVD) and third order (third order dispersion, TOD). The dispersion due to the diffraction gratings depends also on the angle the beam diffracts off the gratings; hence this angle must be different in the Stretcher and in the Compressor to balance the RegA's dispersion. The length of the optical path, in the two stages previously described, is the other parameter to adjust , to obtain a transform limited pulse.
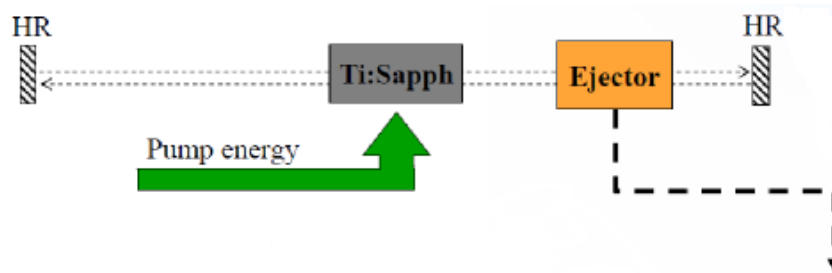
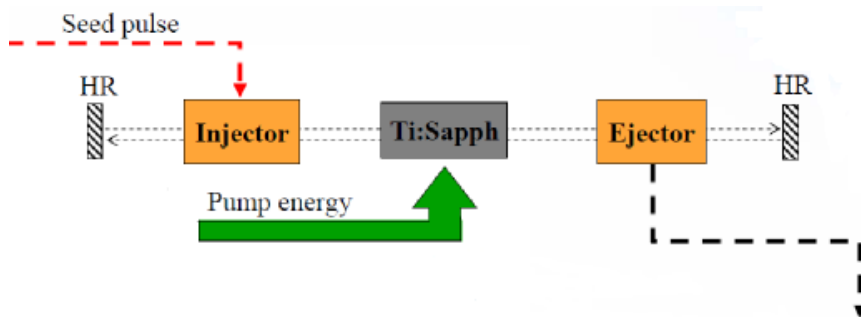Figure 5.6: Regenerative amplifier Q-switch operation

Figure 5.7: Regenerative amplifier seeded operation

5.2.4 RegA 9050

The Coherent RegA Model 9050 is a compact regenerative amplifier system for increasing the pulse energy from the Mira Seed: it requires only a few mW of output power from the oscillator and amplifies this output over 1000 times to the μJ level. The pump source used by RegA is the Verdi laser, the amplification of the Mira Seed's pulses occurs at a repetition rate of 250 kHz (tunable from 10 to 300 kHz). This feature is peculiar of the RegA system, as will be explained in the following.

Let us explain what is a regenerative amplifier by looking at the figures (5.6) and (5.7): when it is pumped (by the Verdi, in our specific case) a

regenerative amplifier behaves like a stand alone laser cavity, it can work in CW or Q-Switched. Figure (5.6) reports the case of Q-Switch, the pump beam induces gain to build up in the Ti:Sa, the regenerative amplifier is working in CW when the ejector is off and finally as soon as the ejector is turned on a pulse is ejected.

A regenerative amplifier can also be used as an amplifier for seed pulses, this is the situation represented in figure (5.7). The injector traps the seed pulse in the cavity, while the pump beam makes gain establish in the active medium. Hence the pulses are amplified at each pass through the Ti:Sa (so at each round trip in the cavity) and finally the ejector allows the pulse to exit the cavity.

The pulse ejection and injection in RegA are performed by an acusto-optic modulator (AOM) that works with high efficiency and so fast that manages to exploit the 3 μs-long energy storage time of the Ti:Sa to produce stable operation at very high repetition rate. Indeed this is the main feature of the RegA: it overcomes the repetition rate limitations associated with the former amplified system based on pulsed pump lasers and electro-optic Pockels cells.
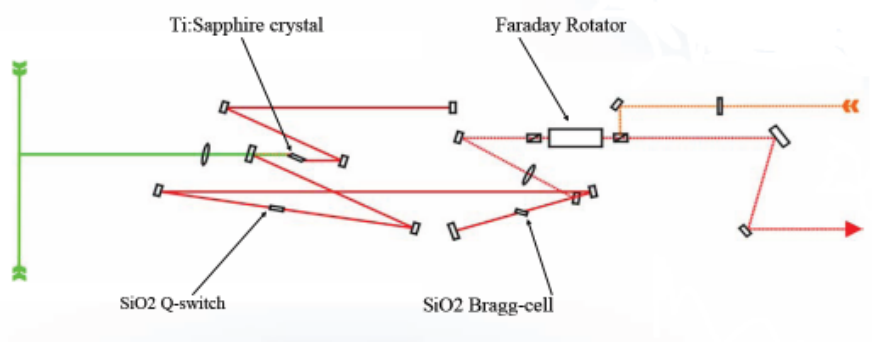

Figure 5.8: RegA 9050 Optical Scheme

The input beam from the Stretcher passes through the Faraday Rotator and a single pulse is injected into the RegA by a SiO_2 acusto-optic Cavity Dumper (it is the AOM and it forms Bragg cell), as is well shown in figure (5.8). Amplification occurs over 20 to 30 round trips, then a single pulse of several μJ energy content is extracted first by the Q-Switch and then by the Cavity Dumper (CD); hence the pulse returns through the Faraday Rotator and is separated from the input beam path by a polarizer. The pulse then exits the cavity in order to be compressed by the Compressor.

The CD and the Faraday Rotator are worth to be described a little deeper. The CD is a SiO_2 crystal that acts as a diffraction grating for the input seed. The refractive index of the CD is modulated by a radio frequency (RF) signal; the repetition rate of the RegA can be varied by changing the RF. There are some photodetectors in the laser head that provide intracavity buildup time and extracted power level signals to the electronic controller for optimization of the RF phase of the CD pulses.
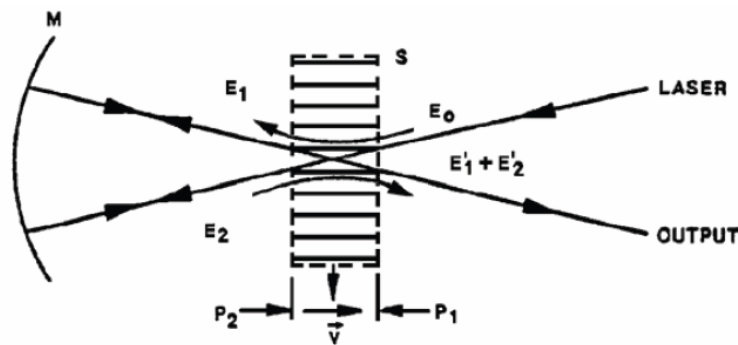

Figure 5.9: Seed pulse injection

The input laser beam is diffracted by the SiO_2 crystal; the optical path of the diffracted beam is a double-pass stage through the crystal, as can be seen in figure (5.9), to obtain an higher diffraction efficiency.

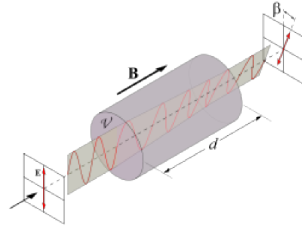The same procedure takes place for the pulse ejection.

Figure 5.10: Faraday rotator

A Faraday rotator is an optical device that rotates the polarization of light due to the Faraday effect; it works because one component of the input light's polarization is in ferromagnetic resonance (i.e. the pulse's frequency equals the precession frequency of the magnetization of the rotator, caused by the torque exerted by an external field) with the material which causes its phase velocity to be higher than the other component's one. The plane of linearly polarized light is rotated when a magnetic field is applied parallel to the propagation direction, as it is reported in figure (5.10).

Faraday rotation is an example of non-reciprocal optical propagation. Unlike what happens in an optically active medium, reflecting a polarized beam back through the same Faraday medium does not undo the polarization change the beam underwent in its previous pass through the medium. This is the reason why the output beam can be separated from the input one with a polarizer, despite of the double pass through the Faraday rotator.

5.2.5 **OPA 9850**

The Coherent Optical Parametric Amplifier 9850 is a wavelength conversion device that converts the RegA output to amplified femtosecond pulses tunable from 1200 nm to 1600 nm (OPA signal) at a 250-kHz repetition rate. At the same time paired pulses with tunable wavelength in the infrared range from 1600 nm to 2400 nm are produced (OPA idler).

M:	Mirror	WP:	Waveplate
D:	Dichroic mirror	Ir:	Iris
L:	Lens	X:	Optical parametric amplifier Beta Barium Borate crystal
S:	Sapphire crystal		
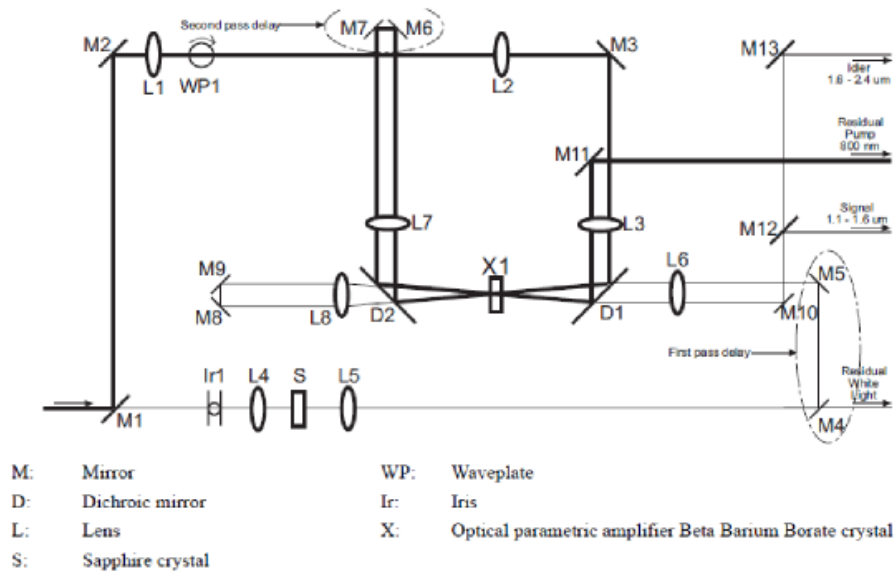
Figure 5.11: OPA optical scheme

An OPA optical scheme is shown in figure (5.3). The 800 nm RegA output enters the OPA and is split by M1 with 75 % of the energy going into the OPA crystal (X1) via M2, passing through a waveplate (WP1), and from M3 to D1. The remaining 25 % passes through on Iris (Ir1) and is focused by the lens L4 onto the Sapphire crystal (S), which produces a whitelight continuum in the 460 − 1600 nm spectral range. The whitelight (WL) is collimated by lens L5.

The WL then passes through an adjustable optical delay (first pass), consisting of M4 and M5. These two mirrors share a common mount that can be moved by an external micrometer so that the optical paths of the WL and 800 nm at optic D1 exactly match.

The 75 % of the incoming RegA beam is steered by M2 and M3 to optic D1 where it is combined with white light from M5 for a first pass trhough the OPA crystal (X1).

At this stage a small amount of signal and idler are generated: the signal is then separated from the 800 nm pump and is reflected by a second fixed optical delay, mirrors M8 and M9. The 800 nm pump is reflected by an adjustable (with an external micrometer) optical delay, mirrors M6 and M7, hence it is recombined with the signal beam at D2 for a second pass through the OPA crystal.

After the second pass the remnant pump beam exits the OPA via output mirror M11. In our set-up the signal and idler are reflected out of OPA with a gold mirror that is encountered by the two beams after the reflection by the M10 mirror. (differently from the scheme in figure 5.11).

The signal wavelength can be changed by angle-tuning the crystal with an external micrometer: this degree of freedom allows to choose from the continuum a different wavelength to amplify for the signal wave.

The crystal of the OPA is a Type II BBO in collinear configuration, this settlement provides more GVM than Type I, therefore shorter crystals are required, but allows to filter easily signal and idler (by their polarization) after the first pass. The Type II BBO is the reason why there is a waveplate (WP1) in the pump's optical path.

We are going to give a brief description of two physical phenomena that occur in this device: Optical Parametric Amplification and whitelight continuum generation.

The Optical Parametric Amplification is a non-linear optical process that involves three waves: the signal, the pump and the idler. Basically the OPA is a Difference Frequency Generation (DFG), so given two input waves (ω_1 and ω_2) they interact in a non-linear crystal, provided certain conditions (i.e. phase matching), and the result is a third wave (ω_3) whose frequency is the difference between the two input waves' ones. So the following relation holds

$$\omega_3 = \omega_1 - \omega_2 \qquad (5.2)$$

In a quantum mechanical approach this equation represents the energy conservation: it is possible to obtain an ω_3 photon only by the annihilation of one ω_2 and one ω_1 photon.

Translating the equation (5.2) for the OPA case we get

$$\omega_i = \omega_p - \omega_s \qquad (5.3)$$

This equation is usually written in the following way:

$$\omega_p = \omega_s + \omega_i \qquad (5.4)$$

The main goal in performing an OPA is getting an intense signal wave at the desired frequency; the idler's generation is unavoidable cause of the energy conservation condition. This doesn't mean the idler is useless, in fact we have uses it to extend the measurements in the infrared region.

Besides the energy conservation there is another fundamental condition to fulfill: the phase matching condition, which represents the momentum conservation.

So

$$k_{\omega_p} = k_{\omega_s} + k_{\omega_i} \qquad (5.5)$$

The phase matching condition is achieved by rotating the BBO crystal, because this means changing the direction of propagation in a birifrangent medium.

The main difference between OPA and DFG relies on the initial conditions, in fact the two input waves in DFG have to be comparable in intensities; otherwise in OPA there is a a pump beam (which is the shorter wavelength one) and a very weak signal beam.

In the OPA the idler beam is generated by the non-linear interaction; actually it is not the only result achieved with OPA. Indeed the amplification of the signal takes place and its intensity reaches the same order of magnitude of the pump's one. Further details about OPA can be found in [5].

As far as the whitelight continuum is concerned it is a non-linear optical phenomenon. The continuum generation process is dominated by self-focusing (SF) and self-phase modulation (SPM), both of which are based on the Kerr optical effect: it consists of a nonlinear dependence of the refractive index on the pulse's intensity.

This nonlinear effect becomes appreciable for high intense fields. In this case we can write

$$n = n_0 + n_2 I \tag{5.6}$$

where n_0 is the usual refractive index, intensity-independent, and I is the laser pulse intensity.

input-beam   optical kerr   output-beam
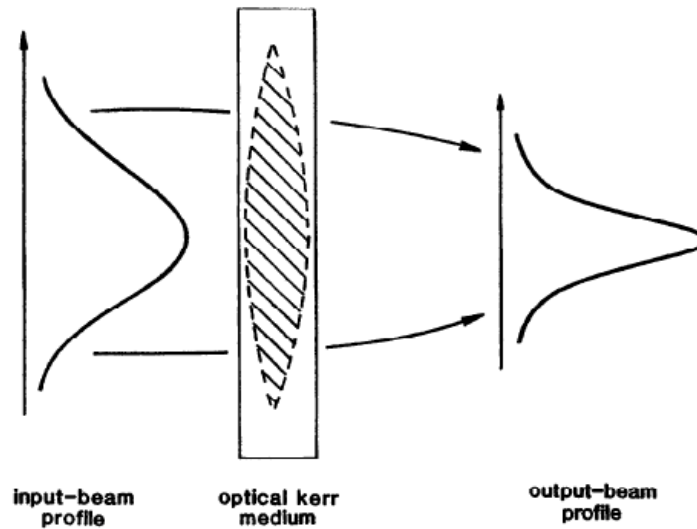profile   medium   profile

Figure 5.12: Beam self-focusing in a Kerr medium

Self-focusing is the nonlinear optical effect in which the laser beam intensity leads to a significant increase in the local index of refraction in the material. The spatial variation in intensity of a Gaussian beam leads to change in index in space and creates a positive lens in the Kerr medium (Sapphire in the OPA) which causes the beam to collapse on itself (fig. 5.12).

The phase of a traveling wave in a dispersive medium of length L is $\phi = nkL = n2\pi L/\lambda$. Let us consider a Gaussian pulse, so the intensity has the following spatial structure: $I = I_p \exp[-2(r/w)^2]$, where I_p is the peak intensity, w is the spot size and r is the distance from the propagation's direction. The consequence of equation (5.6) on the pulse's phase is a shift that has the following value

$$\delta\phi = -2\pi \delta n L/\lambda = (-2\pi n_2 I_p L/\lambda) \exp[-2(r/w)^2] \approx (-2\pi n_2 I_p L/\lambda) \times [1 - 2(r/w)^2] \tag{5.7}$$

Hence in first approximation the phase shift $\delta\phi$ can be considered a parabolic function of (r/w), which is equivalent to the previous statement that the Kerr effect induces a positive lens in the medium.

Self-phase modulation is the temporal parallel of the spatial effect of self-focusing. The temporal shape of the pulse creates a rapidly changing refractive index in time, so we can rewrite the equation (5.6) as time-dependent:

$$n(t) = n_0 + \Delta n(t) = n_0 + n_2 I(t) \tag{5.8}$$

In this framework also the phase of the traveling wave acquires a time dependence $\phi(t) = n(t)kL = n(t)2\pi L/\lambda$, and the phase shif is

$$\delta\phi = -\frac{2\pi \delta n(t) L}{\lambda} = -\frac{2\pi n_2 I(t) L}{\lambda} \tag{5.9}$$

If $n_2 > 0$ (the most common case) there is a decreasing of the frequency (redshift) on the leading edge of the pulse

$$\frac{dn}{dt} > 0 \rightarrow \Delta\omega(t) = \frac{d}{dt}\Delta\phi < 0 \qquad (5.10)$$

where it is supposed a $e^{i\omega t}$ pulse's time dependence. Otherwise blue-shift occurs on the pulse's trailing edge. The spectrum of the continuum is not symmetric about the center frequency, because the n_2 non-linearity has a time delay on the order of 10 fs. This implies that the leading edge of the pulse doesn't experience SF or SPM in the same measure of the trailing edge, therefore conversion to shorter wavelengths is favored. The spectrum is so more extended towards the ultraviolet region from the center wavelength than towards the infrared frequencies.

The threshold for continuum generation is less than 0.5 μJ. Above this threshold the energy output at visible wavelengths has been observed to be nearly linear with input pulse energy.

5.2.6 Pulse characterization

The pump and probe technique imposes some constraints on the laser pulses'
temporal and spatial features (see section 5.1), so there are some quantities
that must be known. In particular, we measured the spot size and the tem-
poral duration of the pump and probe pulses. These data allowed us to
calculate some peculiar properties of the laser beam:

- **Pulse energy**

$$E_P = \frac{P}{Repetition\ rate} \tag{5.11}$$

  where P is the average power of the laser beam, detected by a power
  meter.

- **Fluence**

$$F = \frac{E_P}{A} \tag{5.12}$$

  where A is the beam spot area, $A = \pi r^2$ where r is the radius of the
  spot which depends on the focal length of the lens L for the pump and
  of the spherical mirror SM1 for the probe. The spot size is measured
  by the knife-edge technique. The fluence is a measure of the energy per
  surface unit released by each pulse on the sample.

- **Pulse intensity**

$$I_P = \frac{Fluence}{\tau} = \frac{P}{A \cdot \tau \cdot Repetition\ rate} \tag{5.13}$$

where τ is the temporal duration of the pulse, which we measured with the autocorrelation. In order to get numerical values of all these quantities, we need first to know the beam spot size and the pulse duration.

Knife-edge

The output of the laser system has a beam profile Gaussian in shape. In order to measure the laser beam spot size, we used the knife-edge technique.

It consists of slicing the beam with a metallic blade and detecting the transmitted intensity with a photodiode. The blade was mounted on a motorized translator, controlled via software, that moved with 6 μm steps. The measurement was performed placing the blade in the same position of the sample, so that the same focus condition used in the pump and probe measurement was achieved. The detector was placed just behind the blade, to collect the whole transmitted power.

In figure (5.13) is reported the knife-edge measurement, in panels a) and b) we reported the pump beam measurement. In a) the beam profile sliced by the blade and acquired by the photodiode is reported. The shape obtained is equivalent to a convolution of a Gaussian function (the pulse's intensity) with a step function (the blade); the integration is performed by the photodiode. The real Gaussian profile of the pulse is recovered by differentiating the output of the measurement (i.e. photodiode voltage VS blade position), so we get the result shown in figure (5.13) b). We calculated the spot size by the fit reported in the figure; the Full Width Half Maximum (FWHM) of the Gaussian fit is considered the beam diameter. So the pump diameter results $D = (88.8 \pm 2.1)$ μm.
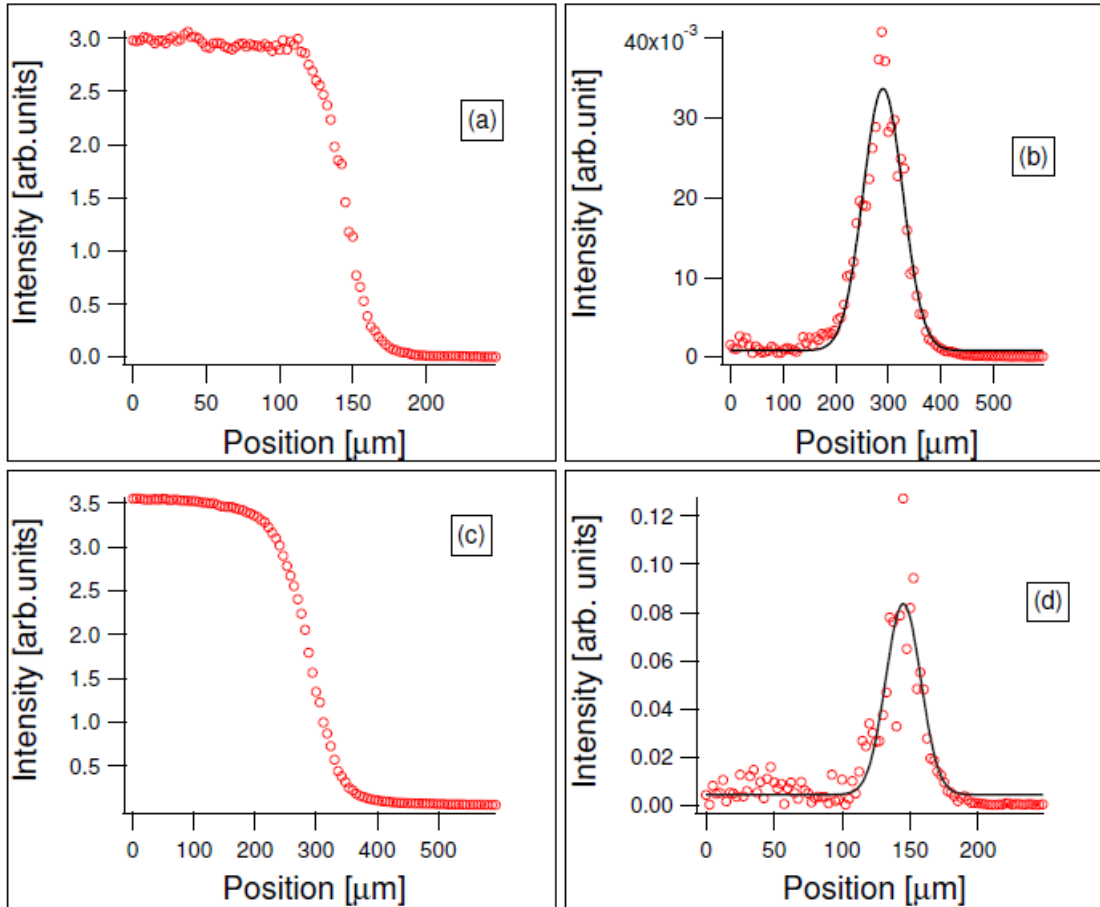
Figure 5.13: Knife Edge measurement: a) Pump beam profile integrated by the photodiode; b) Pump beam profile with Gaussian fit (black line); c) Probe beam profile integrated by the photodiode; d) Probe beam profile with Gaussian fit (black line).

We performed the same measurement on the probe at 1300 nm wavelength. The results are reported in figure (5.13) c) and d). We obtained the value of $D = (30.3 \pm 1.7)$ μm.

This result confirms the choice of the focusing elements (lenses and mirrors). As explained in section (5.1) a necessary condition to perform a pump and probe measurement consists of using as probe a beam with smaller spot

size than the pump's one.

Autocorrelation

The autocorrelation measurement was used to determine the temporal duration of the pump. Phenomena that occur on the femtosecond timescale are out of the detection range of the ordinary electronic devices. That's why another approach is required to determine the duration of the ultra short laser pulses. The time structure of the pulses can be assumed as a Gaussian. The autocorrelation consists in the measurement of the following convolution

$$A(\tau) = \int_{-\infty}^{+\infty} I(t)I(t-\tau)dt \qquad (5.14)$$

The two functions that appear in this convolution are the intensities of two Gaussian pulses equal in temporal width (this explains the name *auto-correlation*) considered at time t and $(t-\tau)$. The integration is performed in the range from $t = -\infty$ to $t = +\infty$ so that the autocorrelation is a function of the delay τ between the two beams.

It is straightforward to get the relationship between the FWHM of the autocorrelation and the FWHM of the input Gaussian pulse. This result allows to determine the duration of the pump pulse by the measurement of the autocorrelation's one. In the case of Gaussian pulses the factor between the two FWHMs is $\sqrt{2}$, it can be easily calculated because only Gaussian integrals occur in the derivation.

The autocorrelation is usually performed by splitting the same beam and then focusing the two components on a non-linear crystal, in spatial and temporal coincidence. The measurement is performed acquiring the second harmonic produced by the input beam. In fact the relationship between the FWHM of the second harmonic and the FWHM of the fundamental wave is very similar to the one previously reported, that comes from the autocorrelation definition (formula 5.2.6).

We performed autocorrelation on the pump beam and cross-correlation measurement between the pump (800 nm) and the probe, tuned in nearly all the range of the OPA.
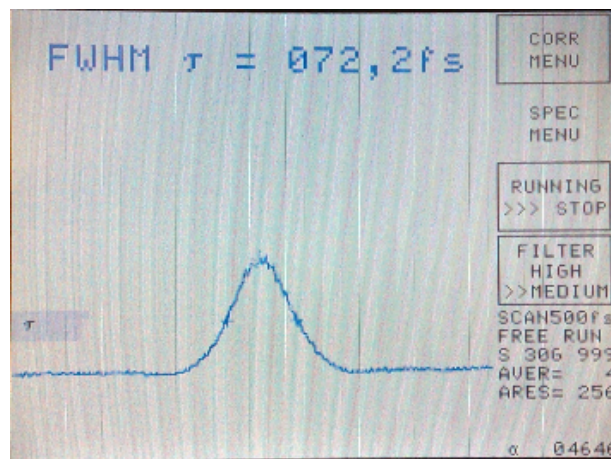

Figure 5.14: Autocorrelation of the pump beam

The result of the pump autocorrelation is shown in figure (5.14); note that the pulse duration value indicated in the picture has to be divided by the deconvolution factor ($\sqrt{2}$), so the pump pulse had a duration of nearly 50 fs.

The cross-correlation of the pump and the probe beams was performed in the following way. A non-linear crystal (BBO) was put in the same position of the sample, then the pump and the probe were directed on the BBO in temporal and spatial coincidence.

The BBO was rotated in the phase matching condition for the Sum Frequency Generation. The crystal has to be rotated to a different angular position everytime the wavelength out of the OPA is changed. The Scan Delay was used to change the delay between the beams (exactly as in the pump and probe technique). The sum frequency signal was blinking, because it appeared when pump and probe were in coincidence and disappeared when the Scan Delay put them out of this condition (i.e. the two beams were separated by a time delay). The signal was finally acquired by a photodiode.

We report the measurement relative to the edge points and a middle point of the spectral range for both the idler and the signal in figure (5.15). We have reported the pulse durations on the figure: the outcome of this measurement is that the temporal duration of the probe pulse is on the order of 100 fs in all the range of OPA. We note that the some experimental traces are not properly fitted by a Gaussian, which means that the laser profile is not very sharp.

Once we have measured the pulse time width we can calculate the pump's fluence. Recalling equation (5.12) we get $F = 1.03$ mJ/cm^2. This result was obtained from a mean power value of 7.98 mW, which corresponds to the 100 % of the pump (pump intensity can be changed with the attenuator). The measured mean power value has to be multiplied by 2, because the chopper actually halves the laser repetition rate by alternating open and
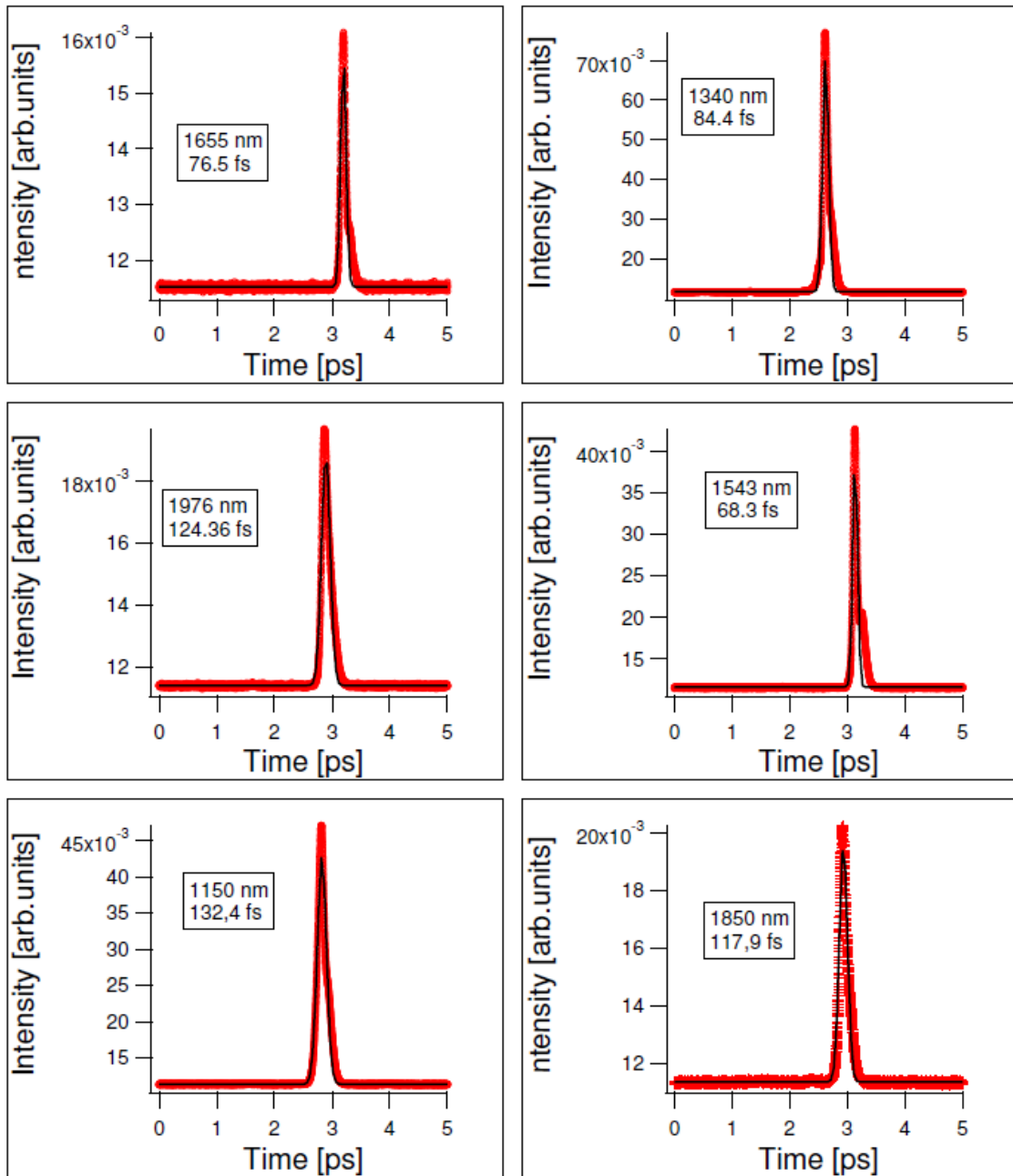
Figure 5.15: Crosscorrelation measurement (black lines are Gaussian fits).

closed windows. The pulse intensity can be calculated by applying equation (5.13), we get $I = 20$ GW/cm^2.

5.3 **Attenuator**

The attenuator is composed by a motorized half-wave plate (that can be rotated via software) and two Brewster windows that act as polarizers. By moving the $\lambda/2$ the polarization of the beam is rotated, so the attenuator's output changes in intensity. The beam reflected by the two Brewster windows exits the attenuator with vertical polarization.
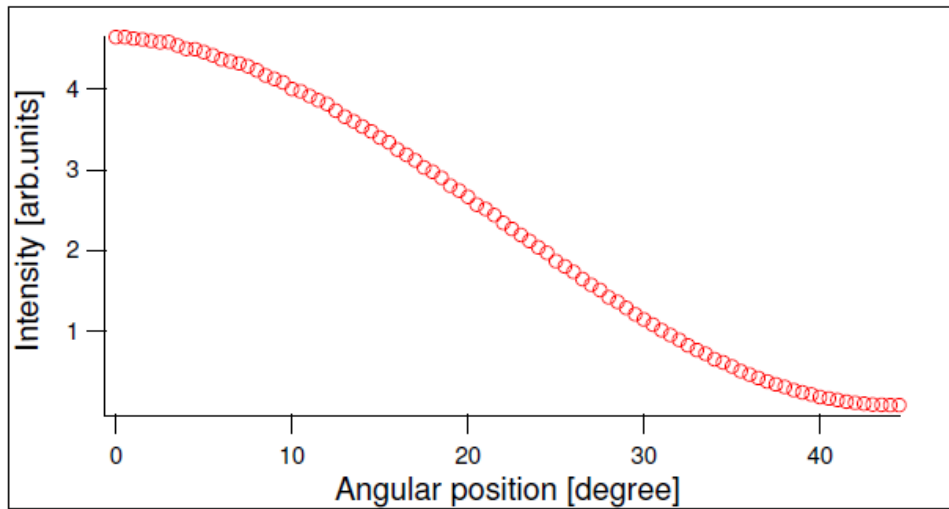

Figure 5.16: Rotator's calibration curve.

The calibration of the rotator is shown in figure (5.16), we performed a scan by rotating the $\lambda/2$ for a 45 degrees range. An angular displacement θ of the halve-wave plate induces a 2θ rotation in the polarization of the input beam.

This result follows straightforwardly from the Jones matrix of the $\lambda/2$, that is

$$
\begin{bmatrix} E_x \\ E_y \end{bmatrix} = \begin{bmatrix} \sin^2\theta - \cos^2\theta & -2\sin\theta\cos\theta \\ -2\sin\theta\cos\theta & \cos^2\theta - \sin^2\theta \end{bmatrix} \begin{bmatrix} E_{x0} \\ E_{y0} \end{bmatrix} \qquad (5.15)
$$

where E_0 represent the electric field of the beam incident on the half-wave plate, while the left hand side of the equation contains the components of the output beam.

Recalling the trigonometric relations:

$$
\begin{aligned}
\sin 2\theta &= 2\sin\theta\cos\theta \\
\cos 2\theta &= \cos^2\theta - \sin^2\theta
\end{aligned} \qquad (5.16)
$$

the 2θ polarization rotation induced by the $\lambda/2$ becomes evident.

So the angular range scanned in the calibration makes the input beam polarization rotating from $0°$ to $90°$. This means that all possible orientations relative to the optical axises can be accessed. The calibration reported in figure (5.16) has been obtained rotating the half-wave plate of a complete period.

5.4 **Lock-in Amplifier**

The lock-in Amplifier used in the set-up is the Standford Research SR830m.
Lock-in amplifiers are used to detect very small AC signals. They use a
technique known as phase-sensitive detection to single out the component
of the signal at a specific reference frequency. Noise signals at frequencies
other than the reference frequency are rejected and don't affect the measure-
ment. Lock-in amplifiers require a frequency reference (ω_r), which in our
set-up comes from the chopper. The signal that enters the lock-in can be
written as $V_{sig} \sin(\omega_r t + \theta_{sig})$ where V_{sig} is the signal amplitude. It is worth
to underline that this expression hold also for signals different from a simple
sinusoidal function; in fact the Fourier's theorem states that each signal can
be decomposed as a sum of sinusoidal terms with different frequencies.

The SR830 generates its own sine wave that can be called lock-in refer-
ence; this signal has the form $V_L \sin(\omega_L t + \theta_{ref})$. Then the signal is amplified
and multiplied by the lock-in reference using a phase-sensitive detector (PSD)
or multiplier. The output of the PSD is simply the product of two sine waves:

$$
\begin{aligned}
V_{psd} &= V_{sig} V_L \sin(\omega_r t + \theta_{sig}) \sin(\omega_L t + \theta_{ref}) \\
&= \frac{1}{2} V_{sig} V_L \cos\left[(\omega_r - \omega_L)t + \theta_{sig} - \theta_{ref}\right] + \\
&- \frac{1}{2} V_{sig} V_L \cos\left[(\omega_r + \omega_L)t + \theta_{sig} + \theta_{ref}\right]
\end{aligned}
\tag{5.17}
$$

The PSD output is formed by two AC signals, one at the difference frequency $(\omega_r - \omega_L)$ and the other at the sum frequency $(\omega_r + \omega_L)$. The output is filtered through a low pass filter in order to remove the AC signals. The only signal surviving is the difference frequency component, i.e. $\omega_r = \omega_L$. In this case the filtered PSD output will be

$$V_{psd} = \frac{1}{2} V_{sig} V_L \cos\left(\theta_{sig} - \theta_{ref}\right) \qquad (5.18)$$

which is a DC signal proportional to the signal amplitude. The PSD and low pass filter detect only signals whose frequencies are very close to the lock-in reference frequency. If the input is affected by noise, noise at frequencies very close to the reference one will result in very low frequency AC outputs from the PSD ($|\omega_{noise} - \omega_{ref}|$ is small). Only the signal at the reference frequency will result in a true DC output and be unaffected by the low pass filter: this is the signal to be measured.

For these reasons we need to make the lock-in reference frequency the same as the signal frequency (i.e. $\omega_r = \omega_L$). Hence not only the frequencies have to be the same, the phase difference between the two signals cannot change in time, otherwise $\cos\left(\theta_{sig} - \theta_{ref}\right)$ will change and V_{psd} will not be a DC signal. This means that the lock-in reference has to be phase-locked to the signal reference, this condition is achieved thanks to a loop called phase-locked-loop (PLL).

As already mentioned the PSD output is proportional to $V_{sig} \cos \theta$ where $\theta = (\theta_{sig} - \theta_{ref})$ is the phase difference between the signal and the lock-in reference oscillator. By adjusting θ_{ref} we can make θ equal to zero, in which case we can measure V_{sig} ($\cos \theta = 1$). Conversely, if θ is 90°, there will be no output at all. A lock-in with a single PSD is called a single-phase lock-in and its output consists of $V_{sig} \cos \theta$.

This phase dependancy can be eliminated by adding a second PSD. If the second PSD multiplies the signal with the reference oscillator shifted by 90°, i.e. $V_L \sin (\omega_L t + \theta_{ref} + 90°)$, its low pass filtered output will be

$$V_{psd2} = \frac{1}{2} V_{sig} V_L \sin (\theta_{sig} - \theta_{ref})$$
$$V_{psd2} \sim V_{sig} \sin \theta$$

$$(5.19)$$

So there are two outputs, one is proportional to $\cos \theta$ and the other to $\sin \theta$. If we call the first output X and the second Y we get

$$X = V_{sig} \cos \theta \qquad\qquad Y = V_{sig} \sin \theta \qquad\qquad (5.20)$$

These two quantities can be thought as the components of a vector (i.e. the signal); X is called the *in-phase* component and Y the *quadrature* component, this is because when $\theta = 0$ X measures the signal while Y is zero.

The phase dependency is removed by computing the magnitude (M) of the signal vector, which results

$$M = (X^2 + Y^2)^{1/2} = V_{sig} \qquad\qquad (5.21)$$

A dual-phase lock-in, such as the one in our set-up, has two PSD's, with reference oscillators 90° apart and can measure X,Y and M directly.

The phase θ can be obtained by the evaluation of

$$\theta = \arctan\left(\frac{Y}{X}\right) \tag{5.22}$$

Hence the lock-in basically multiplies all the components of input the signal by a pure sine wave at the reference frequency. This process occurs every 4 μs, this value represents the working frequency of the lock-in.

In the SR830 lock-in the product of this multiplication yields a DC output signal proportional to the component of the signal whose frequency is exactly locked to the reference frequency. The low pass filter provides the averaging which removes the products of the reference with components at all the other frequencies. So the lock-in measures the single Fourier component of the signal at the reference frequency.

In general the input consists of signal plus noise, which is represented as varying signals at all frequencies. The ideal lock-in responds only to noise at the reference frequency; noise at other frequencies is removed by the low pass filter following the multiplier.

Lock-in amplifiers, as a general rule, display the input signal in Volts RMS (Root Mean Square), it means that when the lock-in displays a magnitude of 1 V the actual signal is $(1 \cdot \sqrt{2})$ V intense.

In our set-up the reference comes from the chopper, the signal is acquired by a photodiode and then enters the lock-in (see figure 5.1). The photodiode is a InGaAs detector, so it has a time-response value typical of the p-n junctions that are in the range of $10-100$ ps. On the other hand, the lock-in cannot deal with spiked input, thus we coupled a 10 kΩ resistance to the photodiode to integrate the signal; the value of the resistance was chosen in order to integrate the laser pulses (emitted at a 250 kHz repetition rate) and not to affect the 13 kHz modulation induced by the chopper.

The signal detected by the photodiode is split into two parts, one enters the lock-in and the other is acquired via computer. The latter contains the data about the reflectivity (R), which we used to evaluate $\Delta R/R$.

We set the integration time of the lock-in to a value of 1 ms; this choice was dictated by the following constraints:

- the integration time has to be larger than the chopper's period, otherwise the lock-in cannot acquire a whole modulation cycle of the chopper;

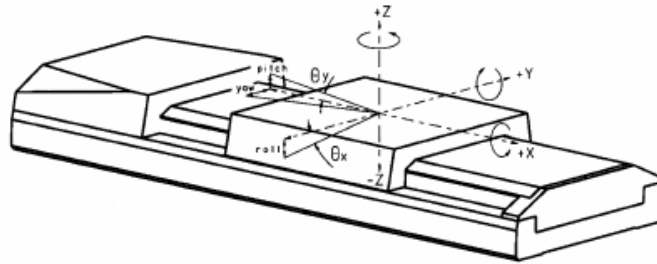- the upper limit is set by the duration of the fast scan (200-500 ms).

Figure 5.17: Sledge

5.5 Scan Delay

The APE Scan Delay is a drive unit for carrying out linear displacements of optical components; in our set-up this device is used for the generation of an optical delay. The optical delay line consists of a motor module and a control electronics module. The former contains the linear drive with the optical element (retroreflector) and the position measuring system. The latter allows to control the optical delay induced on the beam and the time interval (called the *rise time*) required by the device to perform a single scan.

The Scan Delay is mounted on a motorized sledge, represented in figure (5.17), controlled via software.

The Scan Delay is used for the *fast scan* measurements. The total range of the Scan Delay (1-50 ps) has been exploited to measure the fast dynamics in the sub-nanosecond timescale. The choice of the rise time value determines the measurement's resolution and sets a constraint for the choice of the lock-in integration time.

It is interesting to calculate the time resolution of our measurement; the number of representative points is given by the duration of a single scan (that equals the rise time) and the lock-in integration time (see subsection 5.4). A typical rise time value is 0.2 s, so we have 200 points. The actual resolution is obtained by dividing the scan range for the number of the points. Let us suppose to perform a 10 ps scan; in this case our resolution is

$$\frac{10 \text{ ps}}{200 \text{ pt}} = 50 \text{ fs/pt} \tag{5.23}$$

The fast scan technique allows to eliminate the problem of noise on long time scale. For example the oscillations of the laser intensity occur on a time range of 1 hour; the fast scan makes possible to perform a strongly averaged measurement in a much shorter time interval.

It could be possible that the dynamics to study is a longer time scale. In this case the retroreflector is kept fixed and the whole Scan Delay is moved by translating the underlying sledge. This technique (*slow scan*) allows to achieve delays on the order of 2 ns.

5.6 **Cryostat and vacuum system**

The LT-3-110 Heli-tran Liquid Transfer Refrigeration System is used for conductive cooling of small samples in low-temperature experiments in the range from 2 K to 300 K. Cooling is accomplished by the controlled transfer of liquid helium (or nitrogen) through a high-efficiency transfer line to a heat exchanger adjacent to the sample interface. The heat exchanger is hollow and the liquid helium flows in the inside.

The liquid cryogen is transferred through the supply dewar bayonet tube and the transfer line to the cold stage of the refrigerator by externally pressurizing the supply dewar (see figure 5.18). The pressure is 2.5 psig (1 psig $=68.948 \cdot 10^{-3}$ bar) in normal operation regime and reaches the value of 5 psig in the cooling process from room temperature.

Liquid heating is limited during the cooling process by the use of two coaxial pipes in the transfer line: the inner helium flow cools the sample, while the outer works as a thermal insulator.

The liquid flow is regulated by a needle valve at the tip of the refrigerator cold end bayonet. The valve is engaged by an adjustment knob on the transfer line, flow is directed through a heat exchanger in the refrigerator which serves as the interface for the sample holder. A resistive thermofoil heater, tied to the cold stage, allows for sample holder operation above the liquid cryogen's normal boiling point.

The temperature of the cold stage and of the sample holder can be monitored thanks to two cernox sensors connected to a controller (LakeShore 331).
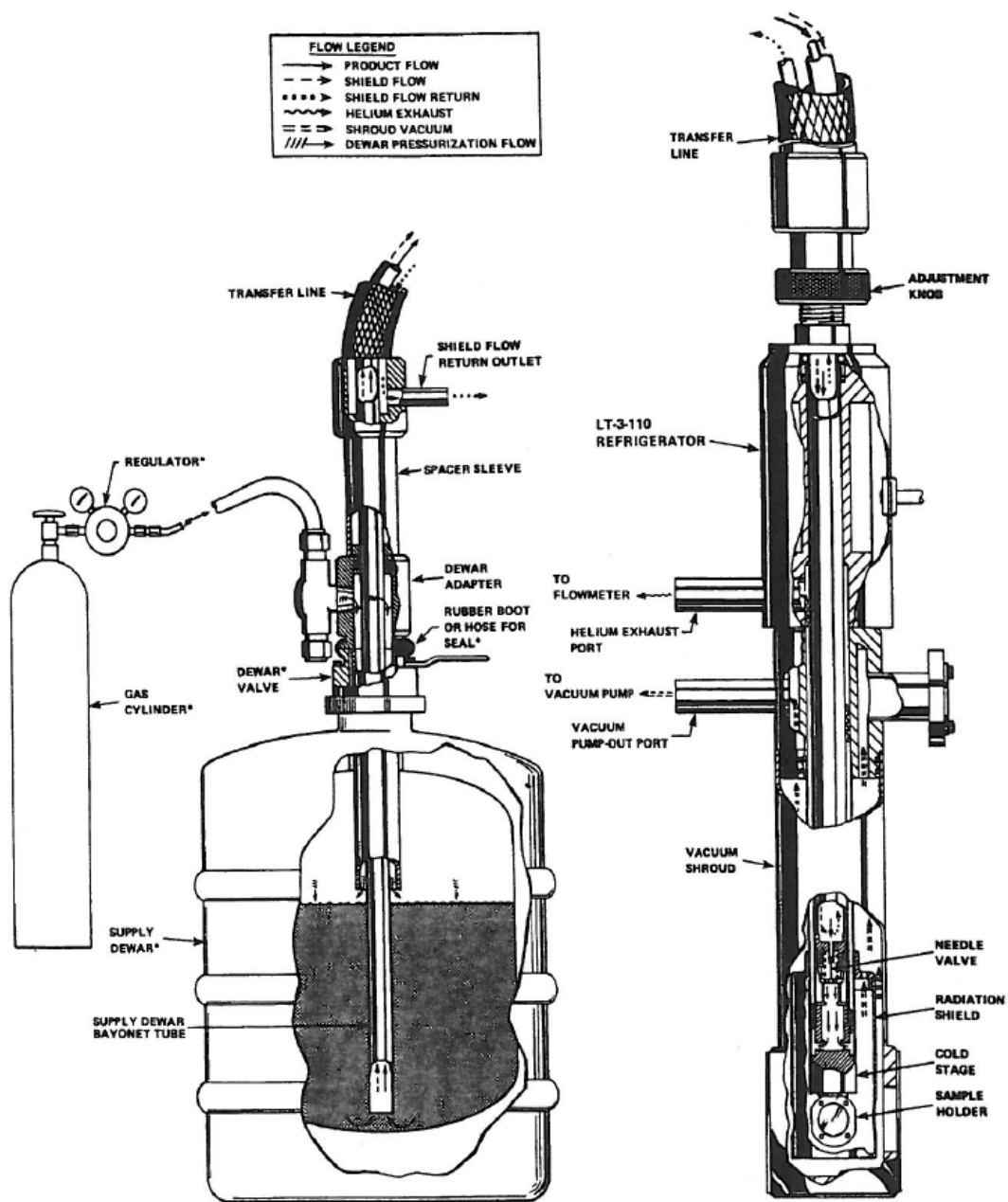
Figure 5.18: Flow diagram

A radiation shield minimizes the radiant heat load on the cold stage, this shield is cooled by helium exhausting from the heat exchanger. The shield has a little window that allows the laser beam to impinge the sample.

The refrigerator must operate in vacuum to eliminate convective heat transfer to the cold internal components in order to keep cryogenic temperatures; the refrigerator in fact was placed in a vacuum chamber.

The pumping system is composed of two pumps from EDWARDS: the pre-pumping XDS Scroll pump, plus the EXT75DX turbomolecular pump. This system let us work in high vacuum conditions at a pressure of $\sim 7 \cdot 10^{-7}$ mbar. These vacuum conditions cannot completely avoid the condensation of impurities (in particular water) on the sample's surface. When the sample has been cooled for some hours (15-20) we can observe a degradation of the reflectivity signal, due to the impurities. The sample had been cleaved before we placed it in the vacuum chamber.
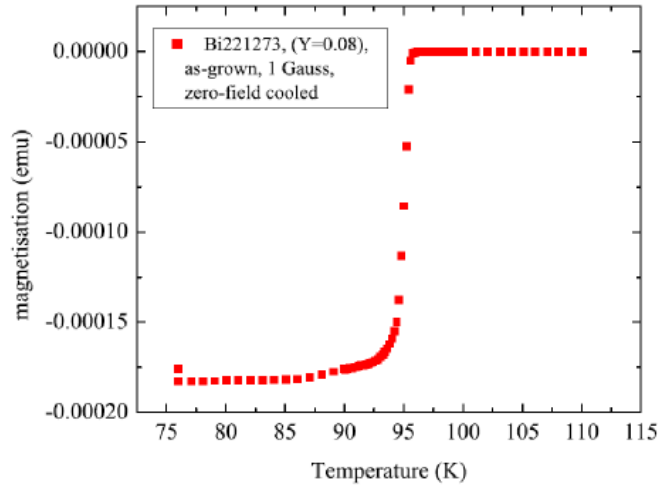
5.7 **Characterization of the sample**

Figure 5.19: Measurement of T_c in Y-Bi2212 OP.

The present work consists of an experimental analysis of optimally doped $Bi_2Sr_2Ca_{0.92}Y_{0.08}Cu_2O_{8+x}$ (Y-Bi2212 OP). The value of the critical temperature has been measured by performing a magnetic susceptibility experiment. When the phase transition which leads the system in the superconducting state occurs, a sudden and sharp change in the susceptibility is observable: in fact superconductivity makes the system diamagnetic. If the temperature of the system is finely changed, while the magnetic susceptibility is measured, a sharp variation of this quantity suggests that the phase transition has just taken place. This procedure allows the precise determination of the critical temperature. Further details about this experimental technique can be found in [2]. The measured critical temperature of the sample is T_c=95 K, as it is shown in fig. (5.19).

6. TIME-RESOLVED OPTICAL PROPERTIES

In this chapter we report the experimental results of this work. The data of the time-resolved reflectivity measurements on the superconducting Y-Bi2212 are shown; the experimental conditions are also described.

6.1 Experimental Data

The goal of this work consists in performing time-resolved reflectivity measurement on High-Tc superconductors, in particular our sample was optmillay doped $Bi_2Sr_2Ca_{0.92}Y_{0.08}Cu_2O_{8+\delta}$ (Y-Bi2212 OP). We acquired the data in the infrared region of the spectrum, in fact the probe used is the OPA (described in section 5.2.5) which works in the spectral range $1200 - 2400$ nm. We performed measurements scanning this spectral region by 50 nm wide steps.

We performed measurements at 15 $\mu J/cm^2$ of fluence. The calculation of the fluence is reported in section (5.2.6).

The total scan range of the Scan Delay (see section 5.5) was 20 ps. The

outcome data are an average of 600 scans, the acquisition lasted about 10 minutes per each wavelength. The signal to noise ratio is 10^5.

These measurement were performed at three different temperatures: 17 K (superconducting state), 100 K (pseudogap state) and 300 K (normal state).

In this section we focus on the data in the superconducting state, since we want to investigate electron-boson coupling in this phase. The results of the measurement in the pseudogap and normal state are reported in appendix (B).

In the upper panel of figure (6.1) we report the $\delta R/R$ signal as a function of the delay, for the different wavelengths. In the lower panel we show a 2D plot of the same data. The discontinuity of the measurements in the 2D plot, between 1550 and 1600 nm, are due to the low OPA signal at degeneracy (i.e. idler and signal have the same wavelength).

Let us look at the single wavelength data (upper panels of fig. 6.1). A sharp change of the signal occurs at zero delay, which corresponds to the pump pulse incidence on the sample. Two different kinds of behavior can be observed from the data. For frequencies between 1100 nm and 1300 nm a positive peak appears at zero delay, then the signal decreases and becomes negative. All the other frequencies show a negative peak at zero delay and all the relaxation dynamics is characterized by negative values of $\delta R/R$.
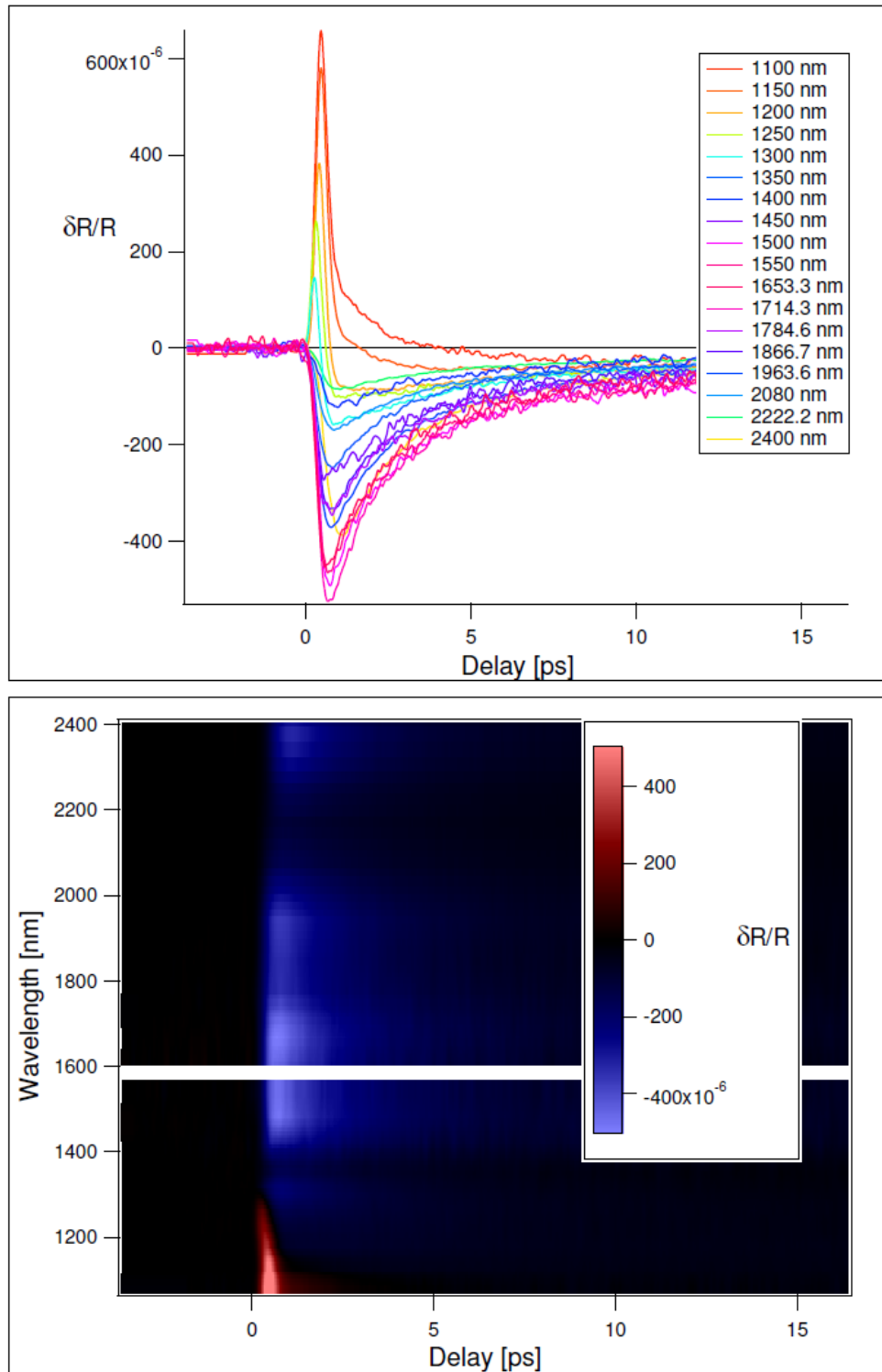
Figure 6.1: Upper panel: single wavelength scans in the whole OPA's range at 15 μJ/cm^2 of fluence (T=17 K). Lower panel: 2D plot of the same data .
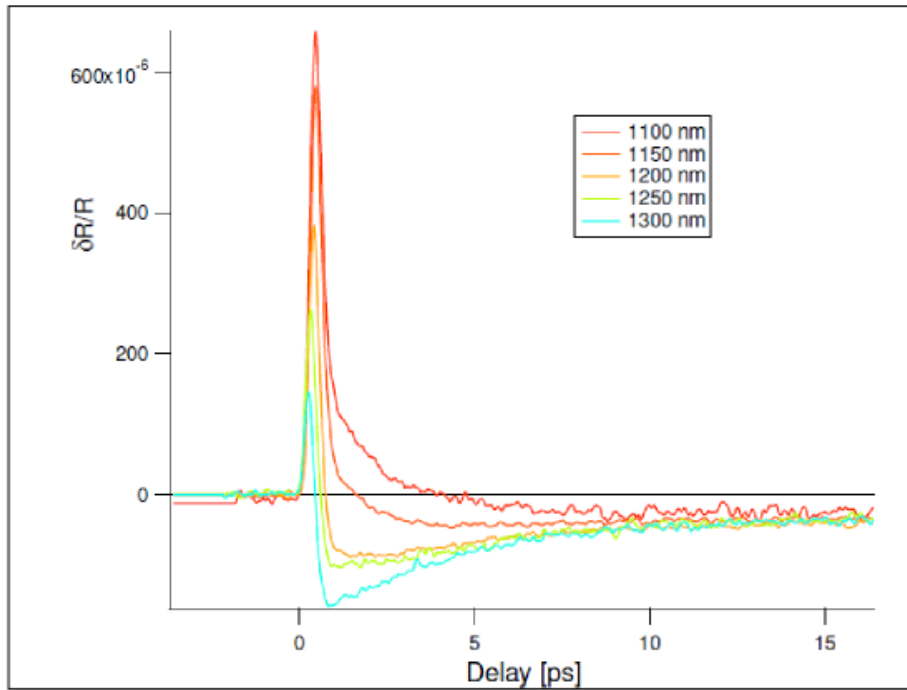
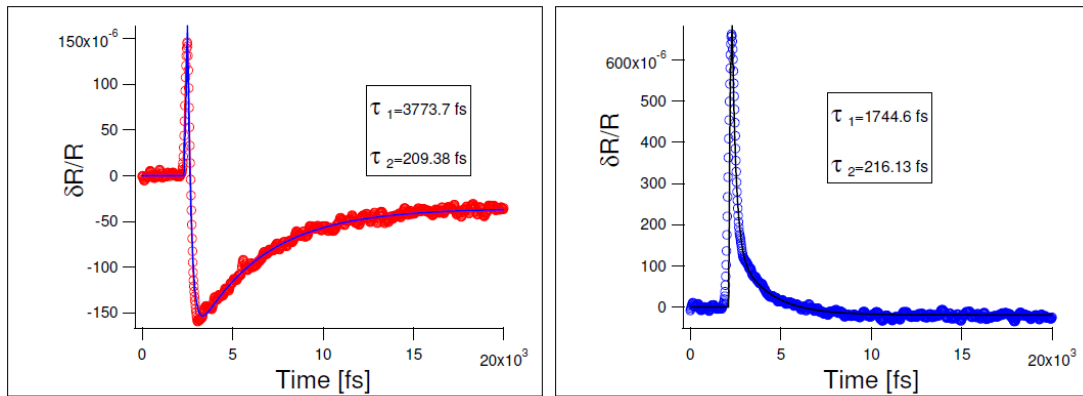Figure 6.2: Single wavelength scans which show a change of reflectivity sign.

Figure 6.3: Fit performed on single wavelength measurements: the fast dynamics is accounted for by the fit. The two wavelengths reported are 1300 nm (left panel) and 1100 nm (right panel), which are the edge values of the spectral range of interest.

The described behaviors are even more manifest in the 2D plots of the data: the red feature corresponds to the positive sharp peak that occurs between 1100 nm and 1300 nm. The change of sign for these frequencies in the reflectivity is clear (passage from red to blue), as the dynamics negative at every delay values typical of all the other frequencies.

We want to focus on the frequencies which exhibits the change of sign in their reflectivity (fig. 6.2). We fitted these data in order to give an estimation of the relaxation dynamics duration. We report in fig. (6.3) the fit performed at 1300 nm (left panel) and 1100 nm (right panel). We chose to show these two particular frequencies because they are the edges of the spectral range of interest.

The fit function contains the sum of two exponential functions, because from fig. (6.3) it looks like that two dynamics contribute to the signal, so

$$H(t)[Ae^{-t/\tau_1} + Be^{-t/\tau_2}] \qquad (6.1)$$

where τ_1 and τ_2 are the decay time of the two dynamics, H(t) is a step function that accounts for the pump pulse impinging on the sample. In principle we should calculate two convolutions of eq. (6.1) with two Gaussian functions: one representing the pump pulse and the other representing the probe. We considered only a single convolution with a Gaussian function, whose temporal Full Width Half Maximum (FWHM) equals the value obtained by the cross-correlation measurement on the pump and the probe. The results of this measurement are reported in section (5.2.6): we use a Gaussian with a 100 fs FWHM.

From the fit we got two decay times on different scales:

	1100 nm	1300 nm
τ_1	(1744.6 ± 78.7) fs	(3773.7 ± 28.7) fs
τ_2	(216.1 ± 5.8) fs	(209.4 ± 1.9) fs

The fast dynamics results on the order of 200 fs, whereas the slow dynamics is in the picosecond timescale.

7. ANALYSIS AND DISCUSSION OF THE RE-SULTS

In this chapter we discuss the data in order to give a physical interpretation to the results. We introduce the theoretical models, that give a description of the non equilibrium dynamics occurring in the sample during a time-resolved experiment. The first is the *two-temperature model*, suitable to describe metals. Then we discuss its extension leading to the *three-temperature model* which can be applied to the strongly correlated materials, like the high T_c superconductors. Finally we deal with the *Rothwarf and Taylor model*, which was proposed to describe the superconducting state for a BCS material; it can be applied also to the cuprates. Then the analysis performed on the data is reported.

7.1 **Two-temperature model**

The dynamics of the excitations photo-injected in a metal in normal state (i.e. T=300 K) can be described by the two-temperature model [23]. The dynamics accounted for by this model is usually covered by the bottleneck in the superconducting state (as explained in chapter 4). This is the reason why the two-temperature description does not apply in this case.

The two-temperature model describes the physics of a pump and probe experiment. The initial temperature of electrons and lattice (i.e. phonons, in a quantum mechanical picture) is the same, so the system in an equilibrium state.

When the pump pulse impinges the sample's surface, the electronic temperature (T_{el}) is suddenly raised up, whereas the lattice temperature (T_{latt}) is left unchanged. The system is out of equilibrium, after some tens of femtoseconds the electrons reach the equilibrium condition among themselves.

Hence the electrons begin to interact with the phonons, until they achieve the same temperature value (i.e. they are in equilibrium): this means that the T_{el} decreases while T_{latt} increases.

After a few hundreds of femtoseconds (200-300 fs) the electrons and the phonons are in equilibrium, so the system has globally a temperature value higher than the initial one. Heat diffusion from the surface to the bulk leads to the recovery of the initial temperature within several nanoseconds.

The phenomenological two-temperature model describe this physical picture by means of the two following equation

$$
\begin{cases}
C_{el}(T_{el})\dfrac{\partial T_{el}}{\partial t} = I_{ext}(t) - G \cdot (T_{el} - T_{latt}) \\[2ex]
C_{latt}(T_{latt})\dfrac{\partial T_{latt}}{\partial t} = G \cdot (T_{el} - T_{latt})
\end{cases}
\tag{7.1}
$$

where C_{el} and C_{latt} are the electronic and phononic specific heat. $I_{ext}(t)$ represents the external perturbation (i.e. laser pulse in our experiment). These equations describe the temporal evolution of the electronic and phononic temperatures. The factor G represents the decay time of T_e, after the initial external-induced sharp rise. It is of course the same time constant that drives the dynamics of T_{latt}, it is of the order of 200-300 fs as aforementioned.

Considering the physical dimensions of the terms appearing in eq. (7.1) $G = \gamma_{e-ph}C_{el}$ where γ_{e-ph} is the inverse of the time decay, so $\gamma_{e-ph} = 1/\tau$. There is a connection between γ_{e-ph} and the electron-phonon coupling constant λ. This link is provided by the Allen formula (derived in [24]), namely

$$
\gamma_{e-ph} = \frac{3\hbar\lambda < \omega^2 >}{\pi k_B T_{el}}
\tag{7.2}
$$

The coupling constant λ is defined as

$$
\lambda = 2 \int_0^\infty d\Omega \ \alpha^2(\Omega)F(\Omega)/\Omega
\tag{7.3}
$$

where $\alpha^2(\Omega)F(\Omega)$ is the spectrum of the phonons.

By solving eq. (7.1) it follows that the electronic temperature decreases on a time scale of

$$\tau = \frac{\pi k_B T_{el}}{3\hbar \lambda < \omega^2 >} \qquad (7.4)$$

7.2 Three-temperature model

Experimental observation of the electron-phonon coupling in cuprates has been performed both in normal and superconducting state. In the latter case the techniques used are other than optical [28] [27]. The experimental evidence reported in [27], which is relative to a Time Resolved Angle Resolved Photoemission Spectroscopy (TR-ARPES) experiment on Bi2212, shows two dynamics appearing in the decay process of the electronic temperature (T_e) following the sharp increase due to the pump pulse excitation. A drop of T_e occurs in $\sim$ 100 fs, which is followed by a decay lasting several picosecond. The slower relaxation has not been observed in usual metals but has been reported in anisotropic materials.

The interpretation provided by the authors is sketched in fig. (7.1). Two subset of phonons have been considered:

- a limited number of modes, which interacts more strongly with the electrons (*hot phonons*);

- a complementary group of nearly non-interacting phonons (*cold phonons*).
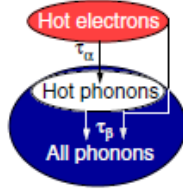
Figure 7.1: Sketch of the energy transfer during the relaxation process. Hot electrons generate hot phonons with characteristic time τ_α, while hot phonons dissipate their energy on a time scale $\tau_\beta \gg \tau_\alpha$.

Electrons transfer energy to the phonons that are more strongly coupled with characteristic time $\tau_\alpha = 110$ fs. This small subset of phonons acquires a temperature $T_p > T_l$, where T_l is the lattice temperature (which is, at this stage, still equal to the initial equilibrium value, like in the two-temperature model). Already after $\tau = 3\tau_\alpha = 330$ fs the hot electrons and hot phonons reach a common temperature (i.e. equilibrium) $T_p \sim T_e$, the dynamics of hot electrons and hot phonons become similar. The electronic cooling can still proceed due to a residual scattering with the cold lattice modes. Moreover the hot phonons are expected to dissipate their energy by means of anharmonic decay. The relaxation by anharmonic cooling and scattering with cold phonons takes place with time constant $\tau_\beta = 2$ ps. After $3\tau_\beta$ the sample surface is in local equilibrium, heat diffusion from the surface to the bulk leads to the recovery of the initial temperature value.

Quantitative description of this physical framework is obtained by an extended version of the two-temperature model, which leads to the so-called three-temperature model [27].

Let us consider the approximation of the hot phonon spectrum $F(\Omega)$ provided by the Einstein model: $F(\Omega) = \delta(\Omega - \Omega_0)$. These modes are coupled

to the electrons through the dimensionless constant

$$\lambda = 2 \int_0^\infty d\Omega \; \alpha^2(\Omega) F(\Omega)/\Omega \tag{7.5}$$

The rate equations describing the temporal evolution of the three temperatures are given by:

$$\frac{\partial T_e}{\partial \tau} = -\frac{3\lambda\Omega_0^3}{\hbar\pi k_B^2}\frac{n_e - n_p}{T_e} + \frac{P}{C_e} \tag{7.6}$$

$$\frac{\partial T_p}{\partial \tau} = \frac{C_e}{C_p}\frac{3\lambda\Omega_0^3}{\hbar\pi k_B^2}\frac{n_e - n_p}{T_e} - \frac{T_p - T_l}{\tau_\beta} \tag{7.7}$$

$$\frac{\partial T_l}{\partial \tau} = \frac{C_p}{C_e}\frac{T_p - T_l}{\tau_\beta} \tag{7.8}$$

where n_e and n_p are Bose-Einstein distributions ($n_{e,p} = (e^{\Omega_0/k_B T_{e,p}} - 1)^{-1}$) evaluated at T_e and T_p, P is the laser energy density. In the rate equations there are also the electronic specific heat (C_e), the hot and cold phonons specific heat (C_p and C_l).

Let us pinpoint with f the fraction of total modes that are strongly coupled. Electron-phonon scattering with the $(1 - f)$ lattice modes, that are weakly coupled, barely contributes to the temporal evolution of T_e and has been therefore neglected. In [27] an estimation of f is reported, it results $f \sim 0.2$. It follows that the 80% of the phonon modes have very weak interaction with the electrons. Two reason can explain this issue

- only a few branches of phonons are significantly coupled;

- the interaction is highly anisotropic.

In conclusion experimental evidences have revealed that the description provided by the two-temperature model is inappropriate for the strongly correlated materials. In these systems the photoexcited carriers may anisotropically and preferentially couple to a subset of phonon modes, resulting in the failure of assignment of a single temperature to the whole lattice structure.

No optical experiment so far has shown the electron thermalization dynamics in the superconducting state; this is the new thing of this thesis work. This evidence allows us to apply the three-temperature model to our data.

7.3 Rothwarf-Taylor model

Rothwarf and Taylor proposed [25] a phenomenological model, suitable to describe the dynamics of the superconductvity recovery in a non-equilibrium system. This is exactly the physics that lies under a pump and probe experiment performed on a superconductor in the superconducting state.

The model relies on two nonlinear differential coupled equations, which describe the temporal evolution of the quasiparticle and high frequency phonons ($\omega > 2\Delta$, where Δ is the superconducting gap) populations.

The Rothwarf-Taylor equations were originally suggested for BCS superconductors, that's why the quasiparticle-phonon interaction is taken into account. The phonon contribution in this model is not related to a particular phononic branch, it is a general phonon.

The physical process described by the Rothwarf and Taylor model is shown in figure (7.2): the pump pulse breaks some Cooper pairs, thus
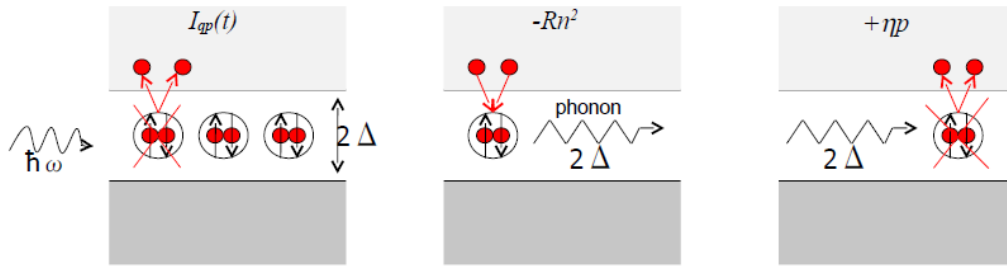
Figure 7.2: Superconductivity recovery: these three stages are well described by the Rothwarf-Taylor equations. All these interactions result in a slow dynamics.

fermionic excitations are injected in the system. These quasiparticles tend to recombine, hence they form pairs in order to establish the superconducting state again.

When two quasiparticles recombine in a Cooper pair a phononic radiation is emitted; in fact the two quasiparticles involved in the recombination have to loose an amount of energy equal to 2Δ, which is the binding energy of a Cooper pair. Thus the phonon is emitted for the energy conservation, which means that its energy is 2Δ (so it is a High Frequency Phonon), the HFP is enough energetic to break another Cooper pair. The lifetime of the HFP determines the duration of the superconductivity recovery dynamics: the slower is the decay of these phonons the more Cooper pair get broken. This results in a slowdown of the dynamics, this effect is called *bottleneck*.

The Rothwarf-Taylor model is based on two coupled equations that express the temporal evolution of the quasiparticles and HFP populations, represented by n and b respectively. The equations are

$$\begin{cases} \dfrac{dn}{dt} = I_{qp}(t) + \eta p - Rn^2 \\[2ex] \dfrac{dp}{dt} = I_p(t) - \eta\dfrac{p}{2} + R\dfrac{n^2}{2} - \gamma(p - p_T). \end{cases} \tag{7.9}$$

where $I_{qp}(t)$ and $I_p(t)$ represent the external sources of quasiparticles and HFP respectively; so in our experiment these terms account for the effects of the pump pulse. For this reason $I_{qp}(t)$ and $I_p(t)$ have the same Gaussian temporal profile of the pump pulse. Usually $I_p(t)$ is neglected, because the main effect of the pump pulse is breaking Cooper pairs, so that electronic quasiparticle are injected in the system (i.e. only n is affected).

The rate of recombination with the creation of a HFP is R, whereas η is the probability for pair breaking by HFP absorption. The factors of $1/2$ arise in the phononic equation because one boson creates two quasiparticles; the coefficients η and R are considered time-independent for simplicity. In principle they could depend on the excitation (laser pulse) intensity and on the temperature, by the way it has been reported in [26] that this dependance can be neglected for a certain temperature range.

The parameter γ represents the rate at which the HFP are removed from the system by processes other than pair excitation. Physically γ is governed by the fastest of the two processes: anharmonic decay of HFP (to an energy less than 2Δ, so that they are no more able to break a Cooper pair) and diffusion of HFP into the thermal bath. Even if this last process is usually slow, it is very important in order to bring the system to the equilibrium condition.

In thermal equilibrium at temperature T the number of phonons is p_T

(Bose distribution), so $b - b_T$ is the bosonic over-population due to the re-combination process or to the external perturbation. The term $\gamma(p - p_T)$ represents the bottleneck: it describes the lifetime of the HFP in the system, considering both the overpopulation and the rate of the decay process.

The dynamics of the recombination is determined by the values of the parameters R, η and γ. Suppose that $\gamma \ll \eta$: in this case a HFP would create two quasiparticles more likely than diffuse into the thermal bath. The consequence is that the phonon population increases until a condition of detailed balance equilibrium is achieved, namely $\eta b = Rn^2$. This last equation of course means that the rate of recombination equals the quasiparticles creation's rate.

When this condition is achieved the two populations are strongly coupled, so they have a slow dynamics featured by the common parameter γ. In this framework the decay of the quasiparticles results to be slow, this trend (imposed by the detailed balance condition) is called *bottleneck regime*. There are obviously other regimes, for example no bottleneck is observed if $\gamma \gg \eta$. The step required to achieve the detailed balance condition is called *prebottleneck*. The above description is suitable for BCS superconductors, with the only contribution of the phonons, instead of a broad bosonic spectrum. In the case of the high T$_c$ superconductors there is an open issue concerning whether the cuprates are in the bottleneck regime (like the BCS materials) or not. In this second case the relaxation process is driven by different interactions, like the bi-particle recombination [29].

We mention the work of Kabanov [26] in which he found analytical solutions to the Rothwarf-Taylor equations in different regimes; he also com-

pared these solutions to the experimental data. Kabanov's claim is that the cuprates belong to the bottleneck regime, like the BCS materials.

7.4 Data Analysis

From the data reported in section (6.1) we noticed that some frequencies show a change in the reflectivity sign. We want to study the dynamics related to this frequency shift of the zero value of $\Delta R/R$ at different delays.

For this reason we performed the following data analysis: we divided the delay axis of the 2D plot of fig. (6.1) in 20 fs width vertical slices, then we acquired the average values of $\Delta R/R$ for each wavelength over this time window. This procedure allowed us to find out which frequency has a vanishing value of the reflectivity variation at every delay, as shown in fig. (7.3).

Then we plotted the extrapolated values of the wavelength versus the delay. We obtained the graph shown in figure (7.4).

We fitted the data with the following fit function

$$H(t)[A(1 - e^{-t/\tau_1}) + B(1 - e^{-t/\tau_2})] \tag{7.10}$$

in which two exponential functions appear, representing two dynamics of time constants τ_1 and τ_2. The term $H(t)$ is a step function that describes the pump pulse incidence on the sample. In principle we should calculate two convolutions of eq. (6.1) with two Gaussian functions: one representing the pump pulse and the other representing the probe.
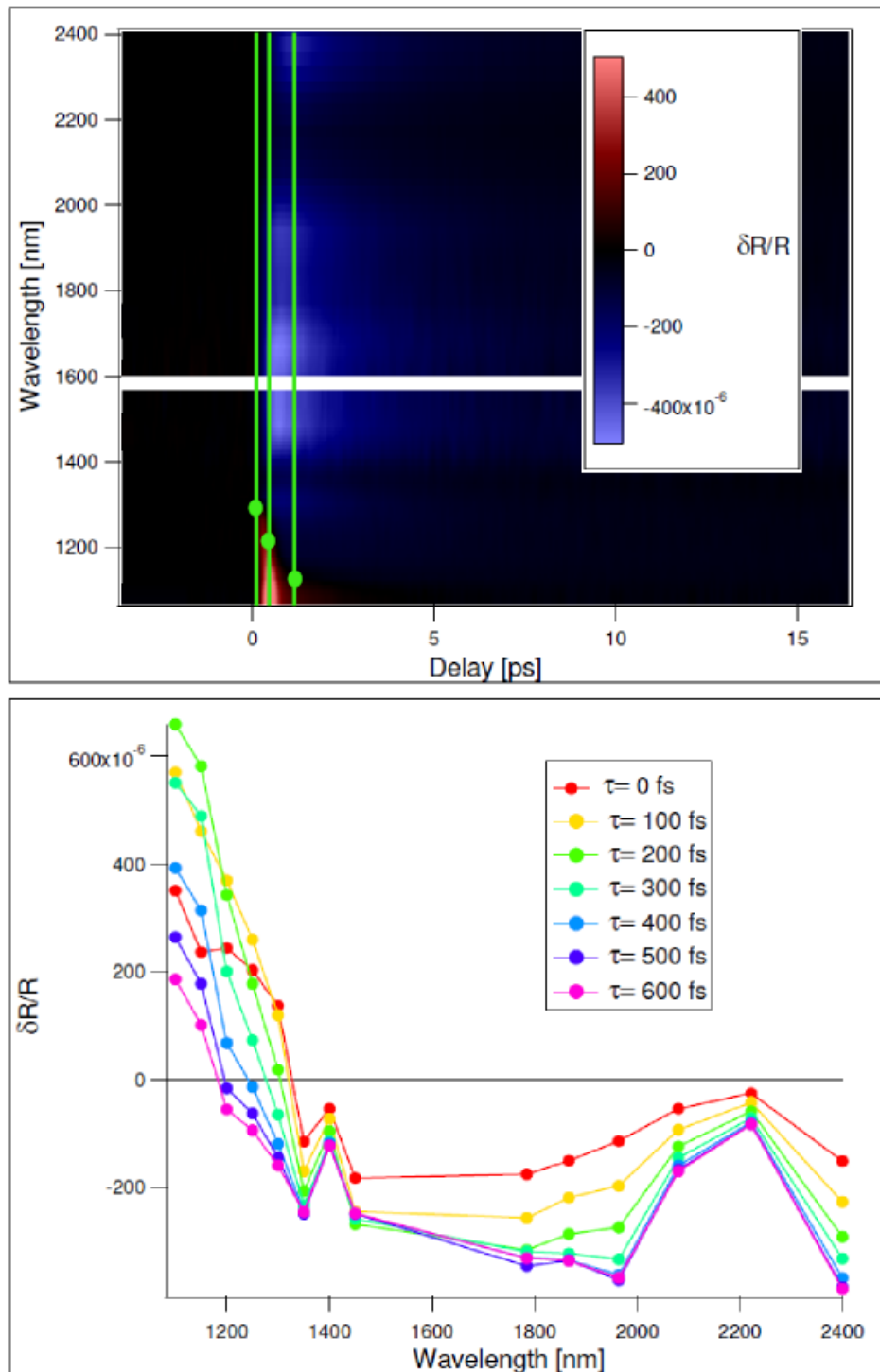
Figure 7.3: Upper panel: 2D plot of the data. The green lines represent some of the 20 fs slices in which we divided the delay axis. The dots are put in correspondence of the reflectivity change of sign. Lower panel: each trace shown represents the average values of $\Delta R/R$ calculated over a single vertical slice. The frequency shift of the reflectivity change of sign is clear.

We considered only a single convolution with a Gaussian function, whose temporal Full Width Half Maximum (FWHM) equals the value obtained by the cross-correlation measurement on the pump and the probe. The results of this measurement are reported in section (5.2.6): we use a Gaussian with a 100 fs FWHM. The values of the time constants obtained from the fit are reported in the following table

$\tau_1 = (336.6 \pm 16.4)$ fs
$\tau_2 = (1.9 \pm 0.6)$ ps

In order to give an interpretation to these values, we performed a numerical simulation based on the three-temperature model (see section 7.2). The result is shown in fig. (7.5): the traces reported were obtained using our experimental conditions as input parameters (reported in the caption). The electron-phonon coupling constant (eq. 7.5) and the frequency of the hot phonon spectrum, considered in the simulation, come from the literature [27].

As shown in fig. (7.5) we fitted the electronic temperature decay dynamics. We used the following function

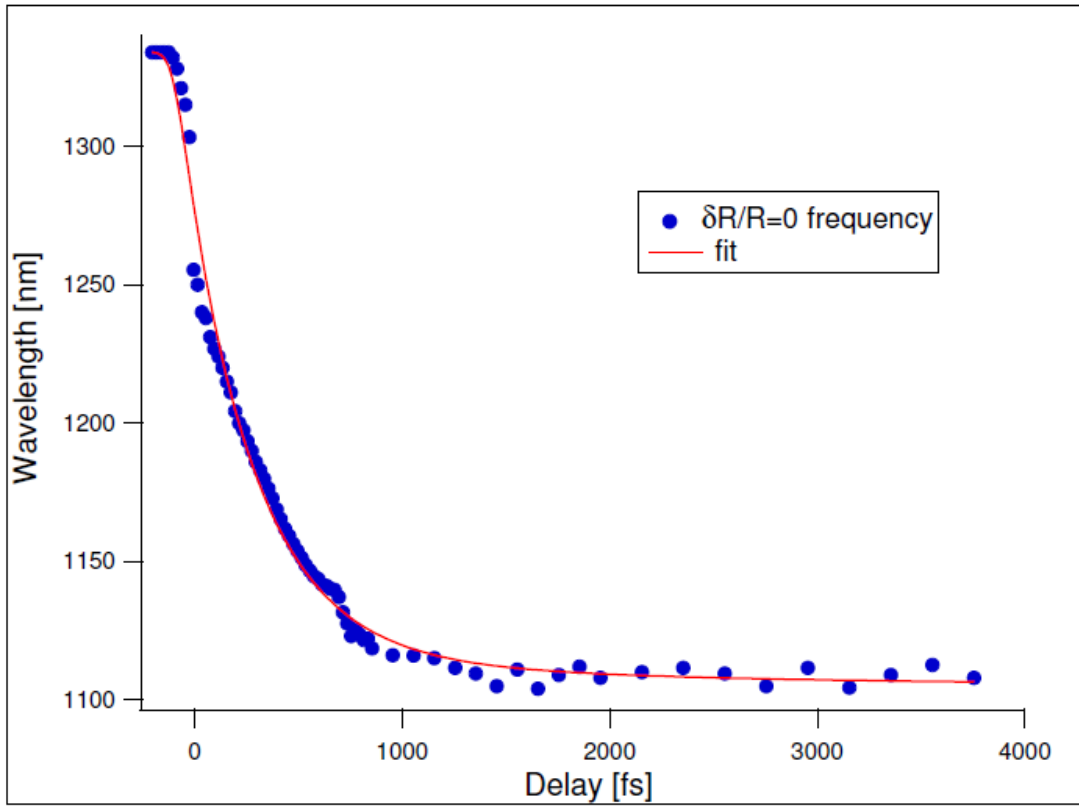$$Ae^{-t/\tau_1} + Be^{-t/\tau_2} \tag{7.11}$$

Figure 7.4: Plot of the frequencies with $\Delta R/R = 0$ extrapolated and put in evidence in fig. (7.3). The red line is the fit performed with the function reported in eq. (7.10).

This two time constants obtained from the fit are

$$\tau_1 = (354.5 \pm 1.3) \text{ fs}$$
$$\tau_2 = (2.2 \pm 0.1) \text{ ps}$$

These decay values are confident with the time constants obtained from the data. This means that the two dynamics, related to the frequency shift of the $\Delta R/R = 0$ point, are accounted for by the three-temperature model. As far as the physical interpretation is concerned, the slower dynamics describes
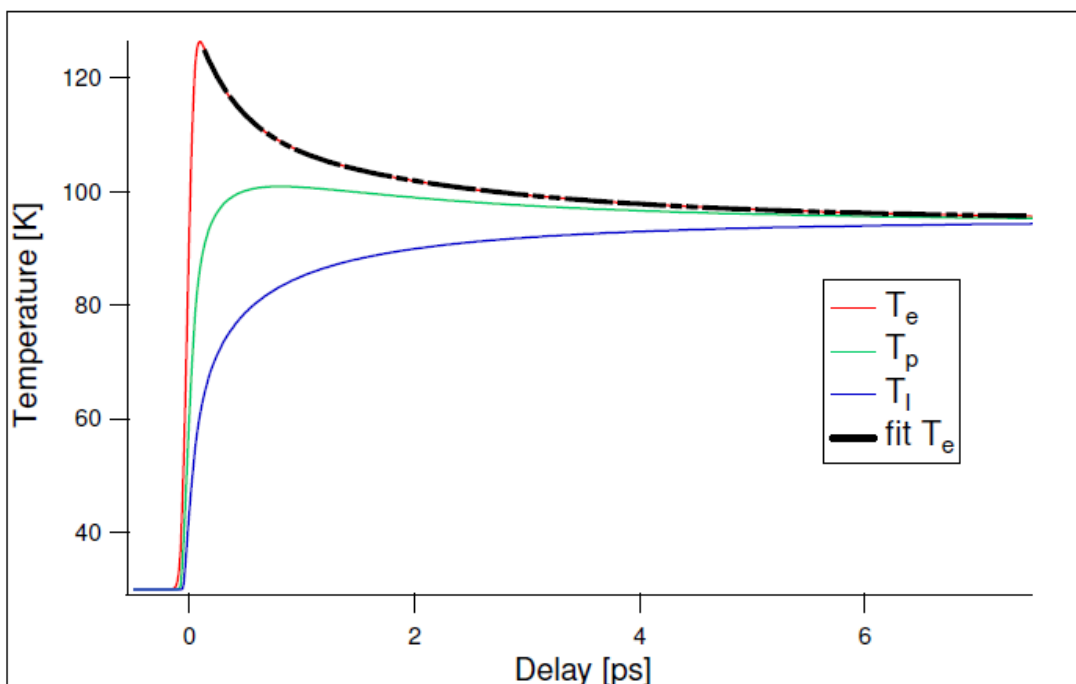
Figure 7.5: Simulation based on the three-temperature model. Input parameters: Fluence=15 μJ/cm^2, T=20 K, $\lambda = 0.07$, $\Omega_0 = 70$ meV, energy density=0.6 J/cm^3. The dashed black line is the fit to the T$_e$ decay.

the thermalization between the cold lattice modes and the hot phonons, which are in equilibrium with the electrons at this stage (see section 7.2).

At the present moment we are not able to give a sure physical interpretation to the fast dynamics: it is related to the thermalization of the electrons with the hot phonons, so to the electron-phonon coupling. However we cannot state wether this process is driven by the the electrons or by the phonons, in fact during the thermalization process both the temperatures (T$_e$ and T$_p$) change simultaneously.

Previously we mention that the electron-phonon coupling constant used in the simulation was taken from the literature. Actually we chose the small-

est value in a range proposed in [27], namely $\lambda = 0.07$. In [15] it is reported the coupling constant between the electrons and the entire phonon spectrum, which is equal to $\lambda_v = 1.53$. The value we used is smaller because it describes the coupling with a subset of phonon modes, whose contribution is not predominant, considering the difference in the coupling constant values.

The three-temperature model (with $\lambda = 0.07$) predicts the same time constants that we actually observed. It means that our experimental evidence is about the interaction of electrons with a subset of phonons, which is not the most coupled in the whole phonon spectrum.

The dynamics related to the more coupled phonon modes should in principle occur on a shorter time scale: considered the difference of two orders of magnitude between λ and λ_v, the femtosecond temporal resolution could not be enough to detect such a fast process.

8. CONCLUSIONS

In this work we have reported the direct observation of a dynamics due to the electron-phonon interaction on superconducting Y-Bi2212 optimally doped, with an optical measurement. This experimental evidence has never been previously reported in the literature.

We noticed a femtosecond dynamics from the data, which is the fingerprint of the electron-phonon coupling.

We interpreted the data in the picture of the three-temperature model, which predicts a trend for the electronic temperature driven by two exponential decay times. These time constants are almost equal to those describing the dynamics appearing in our data.

The slow dynamics can be interpreted as the thermalization process between the hot phonons and the cold lattice modes, as described by the three-temperature model.

The fast dynamics has not a clear physical interpretation yet: the process behind it could be driven by electrons or phonons. A further development of this work consists in performing a differential fit of the $\Delta R/R$ data, by

disentangling the electronic and bosonic temperatures in the Kernel function (see section 3.2). This procedure should allow us to figure out wether the fast dynamics is caused by the variation of the electronic or phononic temperature.

Another possible prosecution could deal with a refinement of the three-temperature model, by taking into account a more realistic phonon spectrum for both the hot and the cold lattice modes.

Moreover it could be very interesting to apply the three-temperature model to the interaction between electrons and spin fluctuations. Considering the combined effect of the phonon and spin fluctuations coupling to the electrons, it should be in principle possible to figure out wether a BCS-like mechanism (considering the interaction between electrons and a broad spectrum of bosons as the pairing glue) can explain the onset of superconductivity in the cuprates.

A. Optical constants

The optical constants are all connected, which means that by knowing only one of them it is possible to calculate all the others. The refractive index is defined as

$$n^2 = \epsilon \tag{A.1}$$

Considering that we are dealing with complex quantities, we have

$$n^2 = (n_1 + in_2)^2 = n_1{}^2 - n_2{}^2 + 2in_1n_2 \tag{A.2}$$

$$\epsilon = \epsilon_1 + i\epsilon_2 \tag{A.3}$$

so we get

$$\epsilon_1 = n_1{}^2 - n_2{}^2 \tag{A.4}$$

$$\epsilon_2 = 2n_1n_2 \tag{A.5}$$

Hence by inverting these formulas we arrive to

$$n_1 = \frac{1}{2} \left[\epsilon_1 + \sqrt{\epsilon_1{}^2 + \epsilon_2{}^2} \right] \tag{A.6}$$

$$n_2 = \frac{1}{2} \left[\epsilon_1 - \sqrt{\epsilon_1{}^2 + \epsilon_2{}^2} \right] \tag{A.7}$$

Besides we can evaluate the optical conductivity $\sigma(\omega)$, which is related to the dielectric function by

$$\epsilon(\omega) = 1 + \frac{i4\pi}{\omega} \sigma(\omega) \tag{A.8}$$

If we are interested in the real and imaginary part we get

$$\epsilon_1(\omega) = 1 - \frac{4\pi}{\omega} \sigma_2(\omega) \tag{A.9}$$

$$\epsilon_2(\omega) = \frac{4\pi}{\omega} \sigma_1(\omega) \tag{A.10}$$

Let us now derive the eq. (3.16), which represents the reflectivity of light at normal incidence onto an interface vacuum-solid surface.

Considering the boundary condition at the interface, for the three waves represented in figure (A.1), we get

$$E_i + E_r = E_t \tag{A.11}$$

where the subscripts i, r and t represent respectively the incident, reflected and transmitted waves at the interface.
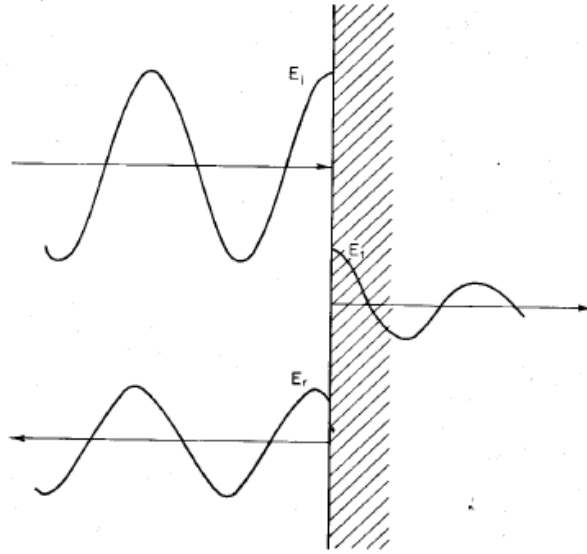
Figure A.1: Illustration of incident, reflected and transmitted waves at vacuum-crystal interface.

Similar conditions hold for H but with a change in sign for H_r. We must remember that $\mathbf{H}$ is orthogonal to $\mathbf{E}$ in the sense that $\mathbf{E} \times \mathbf{H}$ is in the direction of the wave propagation. Thus if E_i and E_r are in the same direction at the interface (see figure A.1), H_i and H_r must be in opposite directions, so that,

$$H_i - H_r = H_t \tag{A.12}$$

In the vacuum $|\mathbf{E}| = |\mathbf{H}|$, whereas in the medium $|\mathbf{H}| = n\,|\mathbf{E}|$ (n is the complex refractive index). So we arrive to

$$E_i - E_r = nE_t \tag{A.13}$$

Eqs. (A.11) and (A.13) are easily solved to yield a reflectance wave amplitude

$$r = \frac{E_r}{E_i} = \frac{1-n}{1+n} \tag{A.14}$$

The reflectivity is then given by

$$R = r^*r = \left|\frac{1-n}{1+n}\right|^2 \tag{A.15}$$

$$= \frac{(1-n_1)^2 + n_2^2}{(1+n_1)^2 + n_2^2} \tag{A.16}$$

Hence this treatment proofs eq. (3.16). This result can be made ϵ dependent

$$R = \left|\frac{1-\sqrt{\epsilon}}{1+\sqrt{\epsilon}}\right|^2 \tag{A.17}$$

Let us now show the calculation of the integral expressed in eq. (3.18). We make use of the eq. (3.11) and we get:

$$\int_0^\infty \omega\epsilon_2(\omega) = \frac{4\pi N e^2 \Gamma}{m} \int_0^\infty \frac{\omega^2 d\omega}{(\omega_0^2 - \omega^2)^2 + \Gamma^2\omega^2} \tag{A.18}$$

$$= \omega_p^2 \Gamma \int_0^\infty \frac{\omega^2 d\omega}{(\omega_0 + \omega)^2(\omega_0 - \omega)^2 + \Gamma^2\omega^2} \tag{A.19}$$

For Γ small, significant contributions come only for $\omega_0 \approx \omega$.

Thus

$$\int_0^\infty \omega\epsilon_2(\omega) = \frac{\omega_p^{\ 2}\Gamma\omega_0^2}{4\omega_0^2} \int \frac{d\omega}{(\omega_0 - \omega)^2 + \Gamma^2} \tag{A.20}$$

$$= \frac{\omega_p^{\ 2}\Gamma}{4} \frac{2}{\Gamma} \left[\arctan \frac{(2\omega - 2\omega_0)}{\Gamma} \right]_0^\infty \tag{A.21}$$

$$= \frac{1}{2}\pi\omega_p^2 \tag{A.22}$$

This result is exact even for interacting many-electron systems, as it is shown in [8].

B. Time-resolved reflectivity data

In this appendix we report the data acquired in the pseudogap state and in the normal state.

Alle the graph shown are relative to measurement performed at 30 μJ/cm^2 of pump fluence. The calculation of the fluence is reported in section (5.2.6).

The delay set by the Scan Delay (see section 5.5) between the pump and the probe pulses was 20 ps, the outcome data are an average or 600 scans.

The pseudogap data don't show any change of sign in reflectivity. Instead in the normal state the usual dynamics well described by the two-temperature model appear.

The white stripe in the spectra corresponds to the degeneracy frequency of the OPA (namely 1600 nm); we weren't able to get enough power from the OPA at this wavelength to perform a measurement.
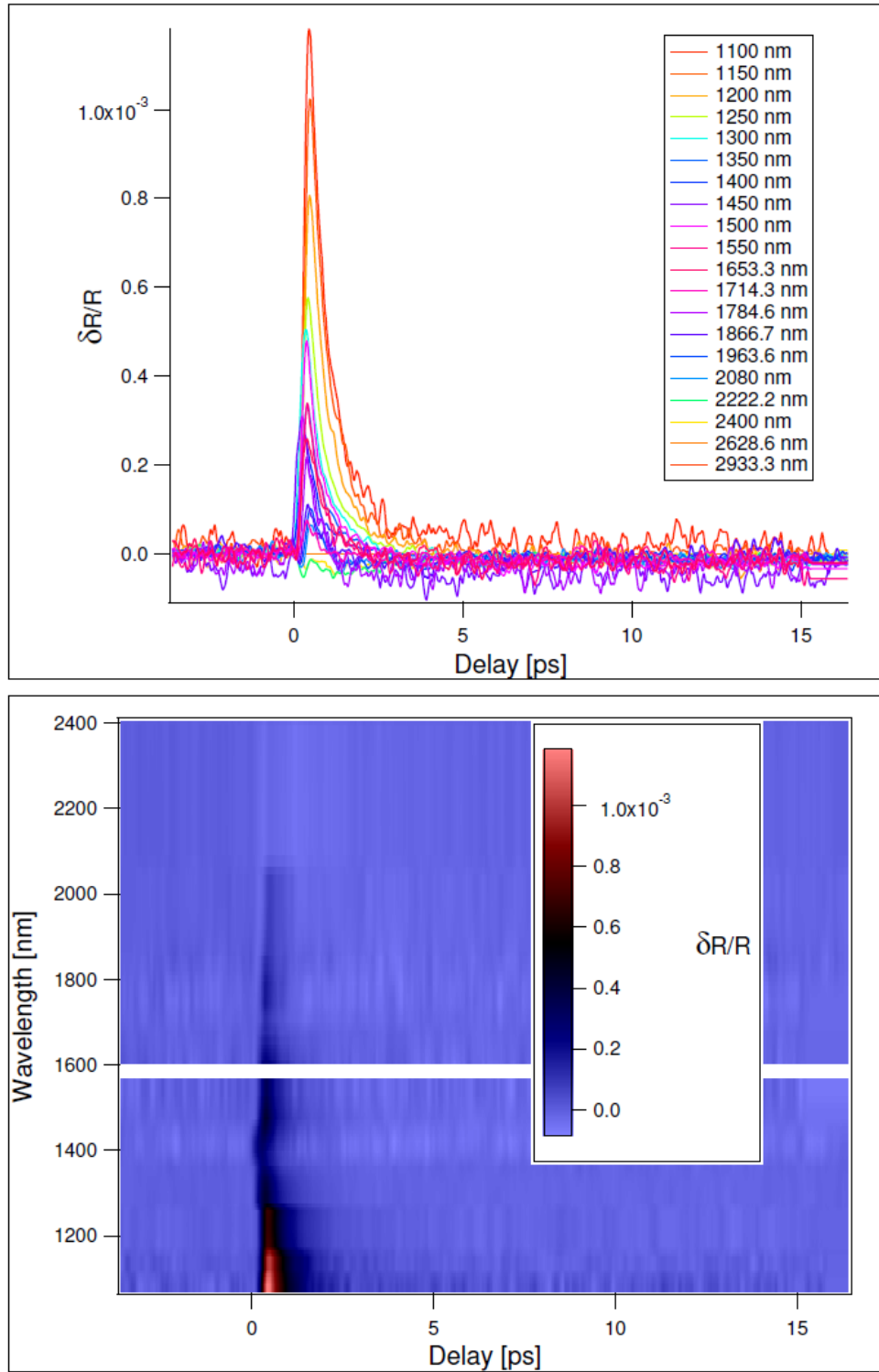
Figure B.1: Upper panel: single wavelength scans in the whole OPA's range in pseudogap (T=100 K). Lower panel: Spectrum acquired in pseudogap state (T=100 K).
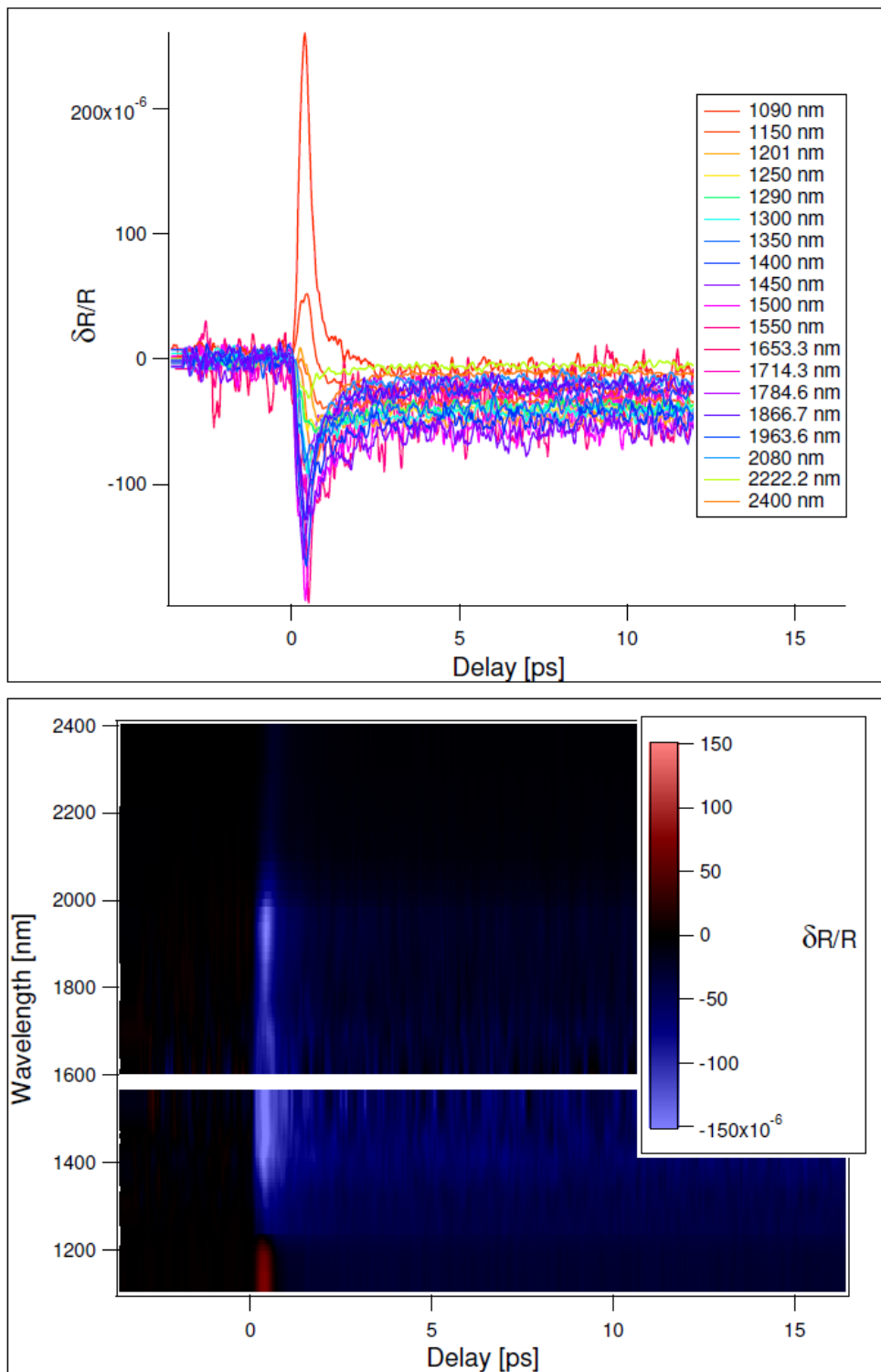
Figure B.2: Upper panel: single wavelength scans in the whole OPA's range in the normal state (T=300 K). Lower panel: Spectrum acquired in normal state (T=300 K)

Bibliography

[1] Federico Cilento, *Dinamiche Elettroniche Fotoindotte in Superconduttori ad Alta Temperatura Critica.*

[2] Giacomo Coslovich, *Dinamiche di non-equilibrio foto-indotte e possibili effetti di transizione di fase in superconduttori ad alta temperatura critica.*

[3] J. Bardeen, L.N. Cooper, J.R. Schrieffer, *Theory of Superconductivity,* Phys. Rev. **108**, 1175 (1957)

[4] Orazio Svelto, *Principles of lasers.*

[5] R. Boyd, *Non-linear Optics.*

[6] H.J.A. Molegraaf, D. van der Marel et al. *Science* **295**, 2239 (2002).

[7] A.V. Boris et al. *Science* **304**, 708 (2004).

[8] F. Wooten, *Optical Properties of Solids.*

[9] J.E. Hirsch and F.Marsiglio, Physica C **331**, 150 (2000), Phys. Rev. B **62**, 15131 (2000).

[10] M.R. Norman et al., Phys. Rev. B **76**, 220509(R) (2007).

[11] P.B. Allen, Phys. Rev. B **3**, 305 (1971).

[12] S.V. Shulga at al., Physica C **178**, 266 (1991).

[13] D.N. Basov, T. Timusk, Reviews of modern physics, **77** (April 2005).

[14] W. Goetze and P. Woelfle, Phys. Rev. B **6**, 1226 (1972).

[15] E. van Heumen et al., Phys. Rev. B **79**, 184512 (2009).

[16] N. Lin at al., Phys. Rev. B **80**, 161105 (2009).

[17] A. Toschi and M. Capone, Phys. Rev. B **77**, 014518 (2008).

[18] F.C. Zhang and T.M. Rice, Phys. Rev. B **37**, 3759 (1998).

[19] A. Damascelli et al., Reviews of modern physics, **75** (April 2003).

[20] P.A. Lee et al., Reviews of modern physics, **78** (January 2006).

[21] N.B. Brookes et al., Phys. Rev. Lett. **87**, 237003 (2001).

[22] Tommaso Sala, *Misure di riflettività risolte spettralmente e temporalmente su superconduttori ad alta temperatura critica in stato normale.*

[23] S. Anisimov et al., Sov. Phys. JETP **39**, 375 (1975).

[24] P. B. Allen, Phys. Rev. Lett. **59**, 1460 (1987).

[25] A. Rothwarf and B.N. Taylor, Phys. Rev. Lett. **19**, 27 (1967).

[26] V.V. Kabanov, J. Demser et al., Phys. Rev. Lett. **95**, 147002 (2005).

[27] L. Perfetti et al., Phys. Rev. Lett. **99**, 197001 (2007).

[28] F. Carbone et al., PNAS vol.105, no.51, 20161 (2008).

[29] N. Gedikver et al., Phys. Rev. B **70**, 014504 (2007).

[30] E.G. Maksimov, Physics Uspekhi **43**, (10), 965, (2000).

[31] G. Eliashberg, Sov. Phys. JETP **13**, 1000, (1961).

[32] G. Eliashberg, Sov. Phys. JETP **16**, 78, (1963).

[33] P. W. Anderson, Science **235**, 1196, (1987).

[34] V.Z. Kresin, S.A. Wolf, Reviews of modern physics **81**, 481, (2009)

[35] J. Zaanen and O. Gunnarsson, Phys. Rev. B **40**, 7391, (1989).

[36] J. Zaanen, G. A. Sawatzky, and J. W. Allen, Phys. Rev. Lett. **55**, 418, (1985).

[37] D. Pines et al., *The theory of Quantum Liquids*, California 1966.

[38] H. Eisaki et al., Phys. Rev. B **69**, 064512, (2004).

[39] N. Gedik et al., Phys. Rev. Lett. **95**, 117005, (2005).

Ringraziamenti

Vorrei ringraziare il prof. Fulvio Parmigiani, che mi ha dato la possibilità di svolgere questo lavoro di tesi, nei laboratori del Sincrotrone. Anche se la mia permanenza a Trieste è durata solo alcuni mesi ho potuto apprezzare l'attenzione dedicata algi studenti, cosa che non è nè comune nè scontata.

Ringrazio in maniera particolare il mio relatore Claudio Giannetti, che nella scrittura di questa tesi ha tentato (spero non invano) di insegnarmi alcuni principi fondamentali dell'approccio all'attività scientifica, che proprio mi mancavano. Inoltre vorrei sottolineare come nell'arco degli ultimi due anni, attraverso lezioni, esami e tanti altri momenti di confronto l'interazione con Claudio sia stata per me importantissima: le poche cose che so in termini di nozioni e di approccio me l'ha insegnate quasi tutte lui.

Un ringraziamento va a Giacomo Coslovich e Federico Cilento per avermi seguito nell'attività sperimentale; sinceramente credo che più di così non avrebbero potuto aiutarmi, avendo sempre risposto ad ogni mia domanda (più o meno sensata) relativa al lavoro di tesi. A Giacomo devo dire grazie anche per i passaggi in macchina e per le nottate passate ad Elettra tra misure e Red Bull. Ringrazio Federico per la disponibilità totale a darmi chiarimenti sul nostro esperimento, anche fuori dagli orari canonici di lavoro, con sessioni miste di fisica e bicchieri di grappa.

Un sentito grazie anche a Stefano Dal conte, per essere venuto a Trieste e averci aiutato a fare le misure poi inserite in questa tesi, anche se non gli mancava certo lavoro da fare nel suo laboratorio di Brescia.

Vorrei ringraziare tutti gli altri professori con cui ho avuto a che fare in

questi 5 anni, il confronto con loro mi ha aiutato a capire se e come avrei potuto occuparmi di fisica al termine dell'università. In particolare ringrazio il prof. Giuseppe Nardelli, non solo per avermi ospitato per un anno nel suo studio spiegandomi esercizi di metodi (quante volte mi ha fatto "ammazzare la mosca con un cannone" o integrare "extra-pezzi" di funzioni nel piano complesso!) e questioni di teoria dei campi, ma soprattutto per avermi "caldamente invitato" a scegliere un piano di studi a 360°: diversamente ora non avrei un singola idea di vari ambiti molto affascinanti della fisica.

Un sentito e profondo grazie va alla mia famiglia: in questi anni ogni mia reale esigenza, e anche vari capricci, sono sempre stati accontetati al fine di mettermi nelle migliori condizioni possibili di poter affrontare l'attività universitaria. Mi rendo anche conto di non essere stato, soprattutto in questi ultimi mesi, il massimo della presenza e della compagnia: quindi grazie, davvero.

Ringrazio poi i miei compagni di università, perchè insieme abbiamo iniziato a muovere i primi (spero non ultimi) passi nel mondo della fisica. Tra tutti vorrei citare: Marco, mio costante punto di riferimento nello studio universitario, sinceramente non ho mai conosciuto uno studente di fisica così bravo; Raimondo "Mastel" , Stefano "l'elettromagnete" e Giovanni "Lord John", compagni di serate nerd e di non so quanti deliri a sfondo (para)scientifico; Isabella, il Cartel, il Lama e Paolo che nei primi hanni di università mi hanno veramente dato una mano; Anna che, nonostante sia una matematica, è una persona che stimo moltissimo e reputo veramenta amica; Federica per le iniezioni di stima e fiducia a livello personale.

Infine non posso non citare quella che definisco sempre come la mia "sec-

onda famiglia": il Club28. Per me non è solo una società che mi ha dato la possibilità di giocare (nonostante gli scarsissimi mezzi tecnici) e di allenare, ma è un ambiente che mi ha accolto anni fa (quando ancora si chiamava Team Exodus) e in cui ora mi sento più che a mio agio, non solo per il modo di vivere la pallacanestro. Un ringraziamento vivissimo va a tutti: i ragazzi delle giovanili, i miei giocatori-compagni di squadra e dirigenti. In particolare voglio citare Carlo Cotelli, che è la vera colonna portante del Club28: con il suo impegno ha creato un ambiente famigliare, in cui i giocatori e allenatori possono vivere la pallacanestro con serenità. Tra tutte le altre persone ricordo Matteo "Cot" Cotelli che ha condiviso con me la pallacanestro ad ogni livello: giocata, allenata (ricordo il corso allenatori, i clinic del maledetto PAO e i playoff sfiorati l'anno scorso) e tifata, con le trasferte a Milano, Bormio, Siena e Barcellona. Per me è stato un piacere condividere queste esperienze con una persona con cui ho molto in comune (Fortitudo a parte!), ma che soprattutto è uno dei mie più cari amici.